Choosing orientation: influence of cargo geometry and ActA polarization on actin comet tails

Catherine I. Lacayo[a], Paula A. G. Soneral[a], Jie Zhu[b], Mark A. Tsuchida[a], Matthew J. Footer[a,c], Frederick S. Soo[a], Yu Lu[d], Younan Xia[d], Alexander Mogilner[b], and Julie A. Theriot[a,c,e]

[a]Department of Biochemistry, Stanford University School of Medicine, Stanford, CA 94305; [b]Department of Neurobiology, Physiology and Behavior and Department of Mathematics, University of California, Davis, Davis, CA 95616; [c]Howard Hughes Medical Institute, Stanford University School of Medicine, Stanford, CA 94305; [d]Department of Materials Science and Engineering and Department of Chemistry, University of Washington, Seattle, WA 98195; [e]Department of Microbiology and Immunology, Stanford University School of Medicine, Stanford, CA 94305

ABSTRACT **Networks of polymerizing actin filaments can propel intracellular pathogens and drive movement of artificial particles in reconstituted systems. While biochemical mechanisms activating actin network assembly have been well characterized, it remains unclear how particle geometry and large-scale force balance affect emergent properties of movement. We reconstituted actin-based motility using ellipsoidal beads resembling the geometry of *Listeria monocytogenes*. Beads coated uniformly with the *L. monocytogenes* ActA protein migrated equally well in either of two distinct orientations, with their long axes parallel or perpendicular to the direction of motion, while intermediate orientations were unstable. When beads were coated with a fluid lipid bilayer rendering ActA laterally mobile, beads predominantly migrated with their long axes parallel to the direction of motion, mimicking the orientation of motile *L. monocytogenes*. Generating an accurate biophysical model to account for our observations required the combination of elastic-propulsion and tethered-ratchet actin-polymerization theories. Our results indicate that the characteristic orientation of *L. monocytogenes* must be due to polarized ActA rather than intrinsic actin network forces. Furthermore, viscoelastic stresses, forces, and torques produced by individual actin filaments and lateral movement of molecular complexes must all be incorporated to correctly predict large-scale behavior in the actin-based movement of nonspherical particles.**

Monitoring Editor
Leah Edelstein-Keshet
University of British Columbia

Received: Jul 1, 2011
Revised: Nov 15, 2011
Accepted: Dec 21, 2011

INTRODUCTION

A large number of infectious microorganisms make a living as intracellular parasites that replicate within the cytoplasm of infected host cells. Some pathogens, including multiple unrelated bacteria and viruses, can employ actin polymerization–based mechanisms to propel themselves within and between host cells by exploiting molecular components from the host cytoplasmic environment and assembling a structure commonly referred to as an actin "comet tail" (Bernardini *et al.*, 1989; Tilney and Portnoy, 1989; Cudmore *et al.*, 1995; Gouin *et al.*, 2005). An actin comet tail is formed from a large number of actin filaments cross-linked in a dendritic meshwork through the activity of the host cell's Arp2/3 protein complex, which nucleates actin filaments and organizes them into a dendritic network (Welch *et al.*, 1997; Mullins *et al.*, 1998; Cameron *et al.*, 2001). Pathogenic bacteria, such as *Listeria monocytogenes* and *Shigella flexneri*, recruit and activate the Arp2/3 complex and initiate local actin polymerization within the host-cell cytoplasm by expressing their surface-bound virulence proteins, ActA and IcsA/VirG, respectively (Kocks *et al.*, 1995; Gouin *et al.*, 1999). Initially, actin from the host cell polymerizes on the surface of these bacteria as relatively symmetrical "clouds" of filaments that eventually

This article was published online ahead of print in MBoC in Press (http://www.molbiolcell.org/cgi/doi/10.1091/mbc.E11-06-0584) on January 4, 2012.

*These authors contributed equally to this work.

†Present address: Department of Biomedical Engineering, Washington University, St. Louis, MO 63130.

Address correspondence to: Julie A. Theriot (theriot@stanford.edu).

Abbreviation used: Ena/VASP, Enabled/vasodilator-stimulated phosphoprotein.

become reorganized into polarized tails that propel these bacteria through the cytoplasm and allow them to spread from cell to cell (Tilney and Portnoy, 1989).

Both ActA and IcsA are expressed on the bacterial surface in an asymmetric manner, with protein density at one pole much higher than at the other; this surface polarity is correlated with the invariable formation of an actin comet tail on the pole that has a higher density of these virulence factors (Goldberg *et al*., 1993; Kocks *et al*., 1993; Smith *et al*., 1995; Rafelski and Theriot, 2006). The polar localization of these two proteins may be responsible for the orientation of bacteria during migration in infected cells: most bacteria migrate parallel to their long axes, and only rarely do the bacteria move sideways (Tilney and Portnoy, 1989; Goldberg and Theriot, 1995; Lauer *et al*., 2001; Soo and Theriot, 2005a). Alternatively, the observed orientation of moving bacteria in host cells may be due to a geometrical or mechanical preference for movement of a rod-shaped particle parallel to its long axis through a viscous environment.

The development of reconstituted motility systems, in which bacteria or artificial cargoes can be propelled by actin comet tails when placed in cytoplasmic extracts or a mixture of purified proteins, has allowed the examination of biochemical and biophysical parameters governing actin polymerization–based motility (Cameron *et al*., 1999; Loisel *et al*., 1999; Bernheim-Groswasser *et al*., 2002; Giardini *et al*., 2003; Upadhyaya *et al*., 2003; Schwartz *et al*., 2004; Soo and Theriot, 2005a). Furthermore, several biophysical models have been established to describe the forces generated by actin polymerization in the comet tail of bacteria (Peskin *et al*., 1993; Mogilner and Oster, 1996, 2003; Gerbal *et al*., 2000a; Dickinson and Purich, 2002; Dickinson *et al*., 2004). The tethered, elastic, Brownian ratchet model and clamped-filament model provide microscopic descriptions of the forces generated by actin polymerization at the surface of the cargo. In the tethered, elastic-ratchet model, the ends of actin filaments attach to the cargo transiently and thus resist the propulsion of the cargo; these filaments then detach and are able to generate a propulsive force (Mogilner and Oster, 1996, 2003). The clamped-filament model proposes instead that the ends of all actin filaments are attached to the cargo via end-tracking motor proteins that repeatedly step to remain bound to the ends of filaments as these elongate and move the cargo forward (Dickinson and Purich, 2002; Dickinson *et al*., 2004). A significant limitation of these microscopic models as originally formulated is that they consider only the force and speed generated by actin growth against a load but ignore cargo shape and trajectory curvature. In contrast, the elastic-propulsion model operates on a larger scale than these two microscopic models and thus considers the overall geometry of the cargo (Gerbal *et al*., 2000a). This model describes a pattern of strain accumulation in the actin comet tail, which is treated as a cross-linked gel, given that the comet tail has been shown to behave as an elastic gel experimentally (Gerbal *et al*., 2000b), and predicts forces that are directed inward, orthogonal to the long axis of the bacterium, creating stresses that are relieved at the back of the bacterium as it moves forward (Gerbal *et al*., 2000a). Consistent with this model, deformable cargoes, such as phospholipid vesicles and oil droplets, are distorted into teardrop shapes by actin comet tails, suggesting the existence of significant stresses orthogonal to the direction of motion (Giardini *et al*., 2003; Upadhyaya *et al*., 2003; Boukellal *et al*., 2004). Within the framework of this elastic-propulsion model, which includes specific assumptions, the geometry of the moving cargo should have a significant effect on force production by actin polymerization, and the actin-based motility of rod-shaped bacteria would be most stable parallel to the long axis simply by virtue of the elongated shape of the bacteria (Gerbal *et al*., 2000a). A recent version of this mesoscopic model represents the viscoelastic actin network as series of particles subject to viscous drag and coupled by springs that break when stretched beyond a threshold (Dayel *et al*., 2009). When this model was simulated under circumstances in which actin-filament depolymerization does not occur—so that stress in the actin gel can be relieved only by network breakage—it gave rise to predictions of movement in an orientation perpendicular to the long axis only (Dayel *et al*., 2009). Unfortunately, most experimental studies on propulsion of artificial particles by comet tails have used spherical polystyrene beads, so the effects of shape and orientation could not be addressed (Cameron *et al*., 1999, 2004; Bernheim-Groswasser *et al*., 2002). However, there is a small amount of tantalizing experimental evidence showing that asymmetric cargoes exhibiting both flat and curved surfaces can form comet tails on any surface, regardless of the local surface curvature (Schwartz *et al*., 2004).

To investigate the contribution of cargo geometry to the typical orientation of rod-shaped bacteria being propelled by actin comet tails, we reconstituted actin polymerization–based motility using ellipsoidal beads uniformly coated with the *L. monocytogenes* ActA protein, which mimicked the overall shape of bacterial rods, while eliminating any possible influence of polarized protein expression. We also examined how ActA mobility and polarization affected motility, and how the placement of the actin comet tail on the surface of ellipsoidal beads changed with variations in motile behaviors. We found that, separately, the elastic or tethered-ratchet models of propulsion by actin comet tails are insufficient to predict the observed behaviors. We propose a combined elastic-ratchet model that takes particle geometry into account and connects quantitative measurements of ellipsoidal bead motility at the mesoscopic scale to biophysical activities of actin filaments at the molecular scale.

RESULTS

Ellipsoidal beads predominantly migrate oriented either parallel or perpendicular to their long axes

For these studies, polystyrene ellipsoidal beads were manufactured to approximate the size and geometrical shape of wild-type, rod-shaped *L. monocytogenes*. These ellipsoidal beads, which exhibited a consistent size (on average 1.8 µm long [SD = 0.3] × 0.8 µm wide [SD = 0.2]; n = 30) and an aspect ratio of ~2 (Figure 1A), were uniformly coated with a functional soluble form of the *L. monocytogenes* ActA protein and assayed for actin-based motility (Cameron *et al*., 1999). Within 2–4 h after addition to cytoplasmic extracts from *Xenopus laevis* eggs, more than 80% of these ActA-coated ellipsoidal beads formed actin comet tails and exhibited robust steady-state motility resembling the movement of *L. monocytogenes* (Figure 1, B–D). Beads appeared to move primarily in either of two distinct orientations: parallel or perpendicular to the long axis of the bead (Figure 1, B–D). To describe the relative orientation of an ellipsoidal bead, we will hereinafter refer to beads as being in the "parallel" or "perpendicular" orientation, when the bead's long axis is either parallel or perpendicular, respectively, to the direction of movement and to the major axis of the actin comet tail. The minor population of beads with intermediate orientations will be referred to as being in the "diagonal" orientation.

Interestingly, migrating ellipsoidal beads would occasionally and spontaneously switch from one orientation to the other. Figure 1D illustrates a bead switching from the perpendicular to the parallel orientation. While most ellipsoidal beads moved in fairly straight trajectories, a few generated slightly curved trajectories, but were seldom observed to change direction dramatically or move in regularly curved trajectories typical of *L. monocytogenes*,

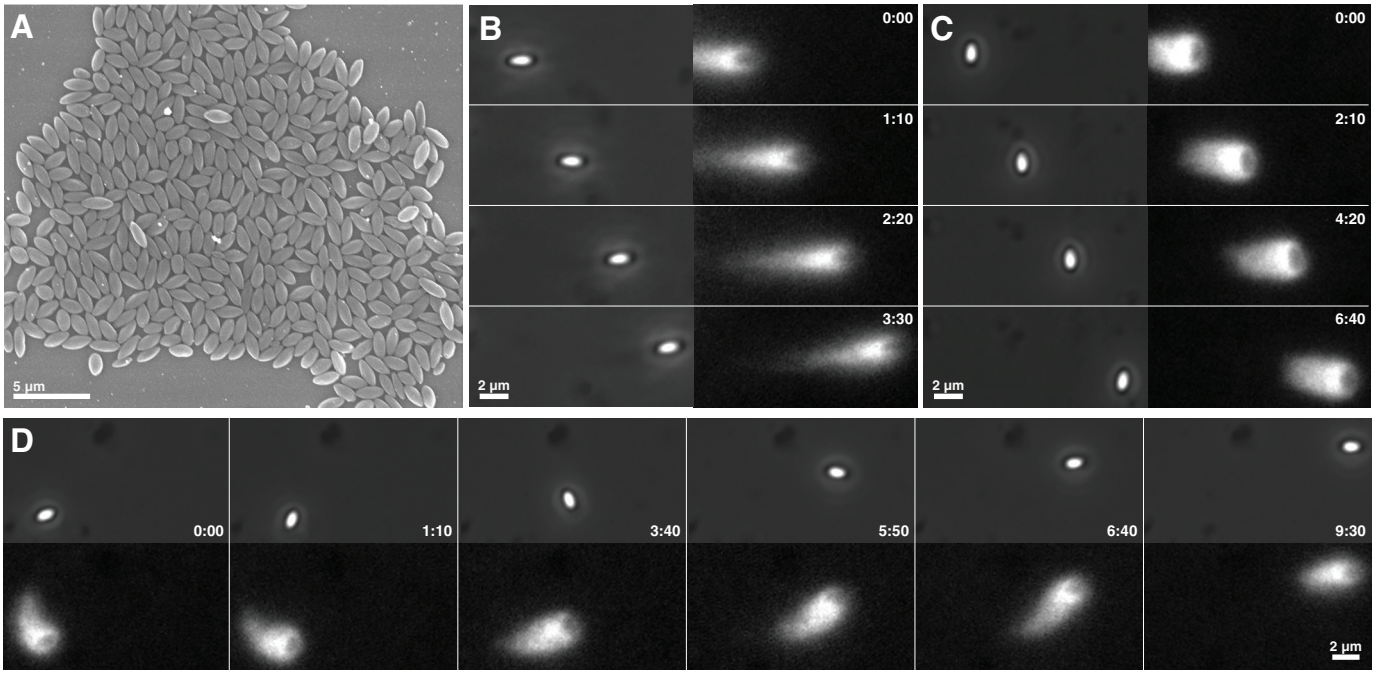

FIGURE 1: ActA-coated ellipsoidal beads display a preference for two distinct orientations when migrating in cytoplasmic extracts. (A) Scanning electron micrograph of the ellipsoidal polystyrene beads used in this study shows their consistent sizes (on average 1.8 µm × 0.8 µm) and an aspect ratio of ~2. Scale bar: 5 µm. (B and C) Beads uniformly coated with ActA and placed in *X. laevis* egg extracts containing fluorescent actin form comet tails and persistently migrate with the long axis of each bead typically oriented either parallel (B) or perpendicular (C) to the direction of motion. Phase-contrast (left column) and actin fluorescence (right column) image pairs are shown. (D) Migrating ellipsoidal beads occasionally and spontaneously switched orientations (in this case, from perpendicular to parallel) or migrated in curved paths. Corresponding phase-contrast (top row) and actin fluorescence (bottom row) images are shown. Scale bar: 2 µm. Time: min:s.

such as sinusoidal, winding "S" or figure-eight curves (Soo and Theriot, 2005b; Shenoy *et al.*, 2007).

Spontaneous motility initiation occurs parallel to the long axis of ellipsoidal beads

It was surprising that ellipsoidal beads appeared to move equally well in both the parallel and perpendicular orientation at steady state. To understand how this distribution of bead orientations was established over time, we compared the frequency of bead orientations relative to their actin comet tails using several hundred still images collected over a 5-h time course. Within 30 min of ellipsoidal beads being added to cytoplasmic extracts containing fluorescent actin, ~10% of the beads counted had developed actin tails, while the rest were stationary and remained associated with actin clouds. The majority of beads started out forming comet tails parallel to the long axis, while beads with tails perpendicular to the long axis were rare at early time points (Figure 2A). By 2 h, most of the beads (78%) were associated with comet tails, and there was an approximately equal fraction of beads in the parallel (Figure 2A, black circles) and perpendicular (Figure 2A, gray circles) orientations. The percentage of beads in the diagonal orientation also peaked by 2 h (22%) and gradually decreased during the rest of the time course (Figure 2A, open circles).

To test the hypothesis that the initial direction of ellipsoidal bead movement was predominantly parallel to the long axis of beads, we examined time-lapse sequences of individual beads undergoing motility initiation or "symmetry-breaking" events. Ellipsoidal beads assembled a thin and nearly symmetrical actin cloud before breaking symmetry, forming a comet tail, and moving directionally (Figure 2B and Supplemental Video S1). All beads observed to spontaneously break symmetry in the absence of obstructions (n = 15/15) started migrating in the parallel orientation. Most of these beads continued moving in the parallel orientation during the first 10 min after symmetry breaking, while a few engaged in at least one orientation switch within that time frame (Table 1). Some beads were observed to initiate movement while in contact with other beads or immediately after a collision with a moving bead. In this scenario, a few beads were able to break symmetry in the perpendicular orientation (Table 1). These data suggest that, during initial comet tail assembly and movement, which predominantly occurred between ~0.5–1.5 h after addition of ellipsoidal beads to cytoplasmic extracts, beads exhibited a strong preference for tail formation and movement parallel to the long axis of the bead, with a low probability of switching orientation within a few minutes of initiating movement. After the initial period of movement (>1.5 h), beads engaged in additional orientation switching until the steady-state distributions of beads moving in the parallel and perpendicular orientation were approximately equal.

Ellipsoidal beads occasionally switch orientation during steady-state motility

After examining the likelihood of orientation switching immediately after motility initiation, we decided to determine how often orientation switching occurred during steady-state motility. Steady-state motility consisted of robust bead movement leading to an approximately equal number of beads in the parallel and perpendicular orientation (2–4 h after adding beads to cytoplasmic extracts). In a large-scale sample of time-lapse sequences in which

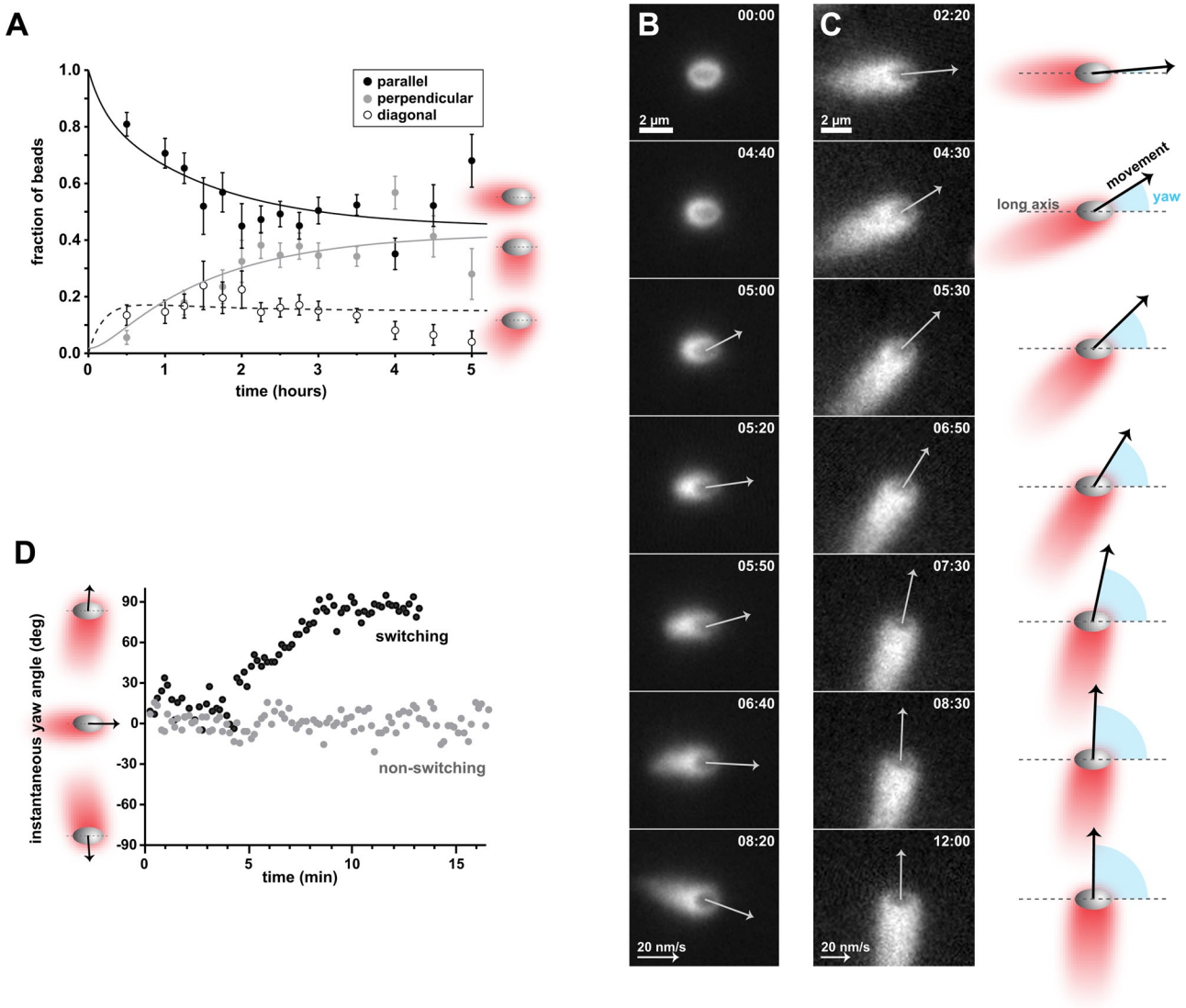

FIGURE 2: Ellipsoidal bead orientation becomes bistable as beads reach steady-state motility. (A) The orientation of ellipsoidal beads was monitored during a time course of 5 h after addition of beads to cytoplasmic extracts. Bead orientation reaches a steady state after ~2 h. Static images were collected, and each bead was classified as having an actin comet tail that extended in an orientation parallel, perpendicular, or diagonal to the long axis of the bead. These comet tail positions relative to bead orientation are schematized on the right. The majority of beads start out moving with comet tails oriented parallel to the long axis (black circles). After 2–4 h, the fraction of beads with tails parallel to the long axis of the bead decreased and that of beads with tails perpendicular to the long axis increased (gray circles), reaching similar levels. Error bars represent SE of the multinomial distribution. Curves represent one possible fit to a differential equation model for reversible conversion between the parallel and perpendicular orientations, with the diagonal orientation (open circles) as an intermediate. (B) Beads spontaneously break symmetry and start moving parallel to the long axis. A representative bead is shown. Spontaneous symmetry breaking occurs in the absence of collisions or interaction with other beads. An ellipsoidal bead is shown in the bead frame of reference: images were computationally translated and rotated so that the bead remained stationary with its long axis positioned horizontally, while the bead's surroundings moved around in each frame of the time-lapse sequences. Arrows depict the direction of movement and the speed of the bead (length of arrow is proportional to speed). Speeds corresponding to Brownian motion and <10 nm/s were omitted. Reference arrow: 20 nm/s. Scale bar: 2 μm. Time: min:s. See also Video S1. (C) Beads can also spontaneously change orientation during migration. This bead switches from moving in the parallel orientation to moving in the perpendicular orientation. The schematics on the right depict the orientation and direction of movement of the bead in each frame. The yaw angle (cyan) is defined as the angle between the long axis of a bead and the vector describing the movement of the bead. The bead is shown in the bead frame of reference as in (B). See also Video S2. (D) The yaw angle is used to quantitatively follow the orientation of migrating beads in time. Yaw angles close to 0° correspond to beads migrating parallel to the long axis, whereas yaw angles close to –90° or 90° correspond to beads migrating perpendicular to the long axis. The yaw angle of a nonswitching bead that migrated parallel to the long axis (gray circles) moderately fluctuated around 0°. The yaw angles of the bead in (C) (black circles) start close to 0° and gradually increase to ~90°, corresponding to the switch in orientation observed in (C).

	Motility initiation							
	Start migrating parallel	1 switch	2 switches	Start migrating perpendicular	1 switch	2 switches	Parallel-to-perpendicular switching events	Perpendicular-to-parallel switching events
Spontaneous (n = 15 beads)	15	5	1	0	0	0	6	1
Collision-induced (n = 20 beads)	17	0	0	3	0	0	0	0
Total (n = 35 beads)	32	5	1	3	0	0	6	1

	Steady-state motility					
	Beads	1 switch	2 switches	Events	Parallel to perpendicular	Perpendicular to parallel
Spontaneous	64	55	9	73	42	31
Collision-induced	35	30	5	40	22	18
Total	99	85	14	113	64	49

TABLE 1: Summary of orientation during motility initiation and switching for uncoated beads.

the steady-state movement of 605 ellipsoidal beads was analyzed, we counted 64 beads that spontaneously switched orientation at least once in the absence of any observable external stimuli. Nine of these beads engaged in a second orientation switch back to their original orientation (Table 1). These observations showed that spontaneous orientation switching was a rare event after beads achieved their stable orientations at steady-state motility. We observed that 58% of the switching events represented spontaneous switches from the parallel to the perpendicular orientation and 42% reflected switching events from the perpendicular to the parallel orientation (Table 1), which is not a significant difference. See Figure 1C for a representative example of perpendicular-to-parallel orientation switching and Figure 2C and Video S2 for an example of parallel-to-perpendicular orientation switching. Collisions and interactions with neighboring beads triggered the orientation switch of an additional 35 beads (Table 1). When these collision-induced bead orientation switches were taken into account, the total bead orientation switching frequencies changed slightly to 57% for parallel-to-perpendicular and 43% for perpendicular-to-parallel switching (Table 1).

To generate a quantitative measure of the orientation of migrating ellipsoids as they switched orientation over time, we calculated the angle between the long axis of each bead and the vector describing the bead's movement. This angle, which we refer to as "yaw angle" (see *Materials and Methods* and Figure 2C) conveyed information about the bead's orientation: small yaw angles close to 0° correspond to beads migrating in the parallel orientation, whereas angles close to –90° or 90° correspond to beads migrating perpendicularly. Yaw angles allowed us to monitor bead orientation over time, revealing moderate fluctuations in bead orientation in short timescales and also large changes in bead orientation during switching (Figure 2D). Switching events were not instantaneous, but usually took place over a period of several minutes, during which time the beads appeared transiently positioned in the diagonal orientation.

Our data suggest that, although the majority of ellipsoidal beads undergo stable motility at steady state, beads are inherently capable of switching orientations at a low frequency. The combination of spontaneous and collision-induced orientation switching observed in our system drives the population from a mostly parallel orientation immediately after symmetry breaking to a balanced distribution in both parallel and perpendicular orientations at steady state. The similar frequency of steady-state beads moving in the parallel and perpendicular orientations, and the approximately equal likelihood of switching in either direction, suggests the two major orientations are energetically and mechanically nearly equivalent, while diagonal orientations are disfavored.

Ellipsoidal beads with laterally mobile ActA typically migrate oriented parallel to their long axes

In the experiments described in the preceding three sections, ActA protein was immobilized on the bead surface (i.e., the attachment points could not move), and the protein was uniformly distributed. Previously, we had found that spherical beads covered with a fluid lipid bilayer prior to ActA coating could also support comet tail formation, but with the interesting modification that ActA protein became polarized to the rear of the bead (Giardini *et al.*, 2003), presumably as the subset of attached filaments pulled the laterally mobile ActA to the rear. A similar colocalization has also been observed between the comet tail and different actin-polymerization activators (based on neuronal Wiskott–Aldrich Syndrome protein) on oil droplets and unilamellar vesicles (Trichet *et al.*, 2007; Delatour *et al.*, 2008). We therefore expected that lipid coating of ellipsoidal beads should change both the lateral mobility of the attachment points and the overall polarity of the ActA protein. Since ActA has been shown to be polarized on the surface of *L. monocytogenes* (Kocks *et al.*, 1993; Rafelski and Theriot, 2006), and the bacteria (unlike uniformly coated ellipsoidal beads) show a marked preference for movement in the parallel orientation, we expected that lipid coating would have a measurable effect on ellipsoidal bead movement.

To determine how ActA localization and mobility affected ellipsoid motility, we permitted lateral mobility of ActA on a fluid surface by coating ellipsoidal beads with unilamellar vesicles containing a lipid bound to purified ActA. These beads will be referred to as "lipid-coated" beads, while beads coated with ActA without lipid will be referred to as "uncoated." When the distribution of fluorescent ActA and actin was measured along the surface of a migrating lipid-coated bead, ActA was observed in a polar distribution that

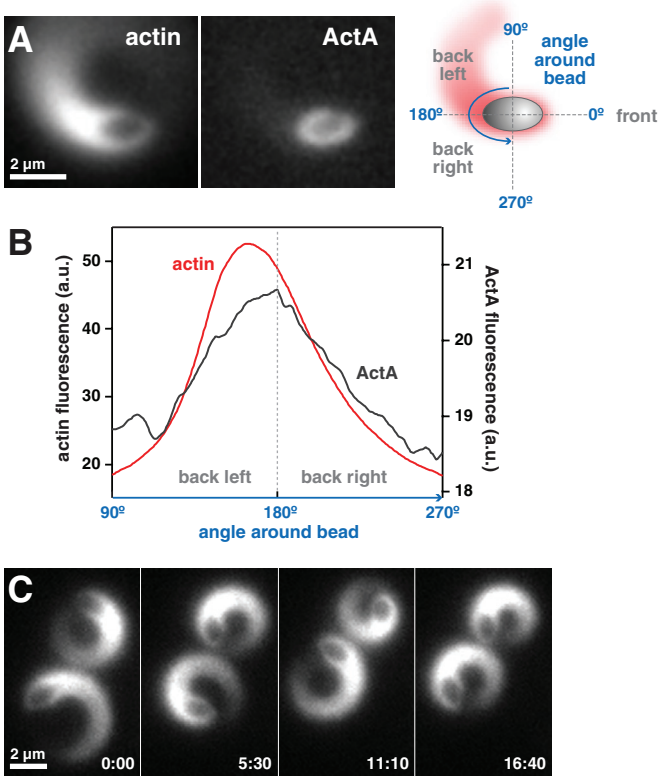

FIGURE 3: Mobile ActA clusters with the actin comet tail and can generate persistently circling ellipsoidal beads. (A) The time-averaged projections of image sequences (actin and ActA) of a curving lipid-coated bead that migrates in the parallel orientation are shown. The average actin and ActA fluorescence on the surface of the bead were measured as depicted in the schematic on the right. Scale bar: 2 μm. (B) The average ActA and actin fluorescence intensities of the bead in (A) are plotted. The angle around the back surface of the bead is plotted on the *x*-axis (left side of the bead: 90°; back of the bead: 180°; right side of the bead: 270°). The distributions of both ActA and actin are asymmetrical, with increased localization on the left of the bead corresponding to the inside of the curve. The motility of this bead is characterized by an average angular velocity of 3.43°/s, average yaw angle of 9.67°, and average speed of 11.7 nm/s. (C) Ellipsoidal beads with lipid-coated surfaces and mobile ActA were often observed to migrate in tight persistent circles. This behavioral phenotype was extremely uncommon for uncoated beads. Scale bar: 2 μm. Time: min:s.

colocalized with the actin comet tail (Figure 3, A and B). When we examined their time-lapse sequences, we found that, unlike uncoated ellipsoidal beads, these lipid-coated beads moved with a robust preference for the parallel orientation (Figure 3A). Lipid-coated beads were also observed to be capable of a novel and striking motility phenotype in which they moved in tight persistent circles (Figure 3C and Video S3), a phenotype not previously reported for artificial particles, but occasionally seen for live bacteria (Lauer *et al.*, 2001; Auerbuch *et al.*, 2003; Soo and Theriot, 2005a; Shenoy *et al.*, 2007). After examining the motion of 165 lipid-coated ellipsoidal beads, we found that 17% of the beads moved in persistent, tight circles, whereas <2% of uncoated beads were able to move in circular trajectories, and these few examples showed less angular persistence than the lipid-coated beads. Other types of complex trajectories, such as S-shaped paths, were also occasionally observed for these beads. Our observations showed that the surface mobility of ActA allowed for its polarization, which correlated with the tendency of ellipsoidal beads to move in the parallel orientation and engage in circling behaviors.

Quantitative analysis confirms the lack of orientation bias observed in uncoated beads and bias for the parallel orientation in lipid-coated beads

To quantify the overall orientation of each bead in the population, we averaged the instantaneous yaw angles obtained from each frame of the sequence containing each bead's trajectory. Overall, the distribution of the magnitude of the time-averaged yaw angles for a large population of uncoated beads (n = 605) was U-shaped (Figure 4A), confirming our qualitative impression of bead orientation. This distribution of average orientations at steady state is consistent with the frequencies of comet tail orientations found after 2 h of adding beads to cytoplasmic extracts during a time course (see Figure 2A). For further analysis, the magnitude of the average yaw angle was used to classify each bead based on orientation. Beads maintaining an average yaw angle of 0°–30° were classified as moving in the parallel orientation, and those maintaining an average yaw angle of 60°–90° were classified as moving in the perpendicular orientation. Based on this classification, 42% of uncoated beads migrated in the parallel orientation, while 47% migrated in the perpendicular orientation (Table 2 and Figure 4A). Moreover, the average yaw angle over the entire population of uncoated beads was close to 45°, reflecting the approximately equal number of beads migrating in each of the two preferred orientations—parallel or perpendicular (Table 2).

In the population of lipid-coated beads (n = 165), the percentage of beads generally migrating in the perpendicular orientation was significantly reduced, such that only 31% of the beads migrated in the perpendicular orientation, while 51% remained in the parallel orientation (Table 2 and Figure 4A). For both uncoated and lipid-coated beads, movement in the diagonal orientation was infrequent, and few beads in the population migrated in this manner when averaged over time (Table 2 and Figure 4A). This smaller group included beads that switched orientation and beads that had slightly curved trajectories.

ActA mobility allows ellipsoidal beads to attain unusually fast speeds and greater trajectory curvature

Our observations thus far allowed us to determine that the nature of the attachment of actin filaments on the surface of beads—that is, mobile or immobile attachment—had significant effects on bead orientation. To determine whether this change in filament attachment affected the motile behavior of ellipsoidal beads, we quantitatively measured and compared the speed and trajectory curvature of uncoated and lipid-coated beads. When we examined speed, we found that, on average, lipid-coated beads migrated significantly faster (by Wilcoxon rank-sum test, $p < 0.001$) compared with uncoated beads (Figure 4B and Table 2). On closer inspection, it was clear that a subpopulation of lipid-coated beads was contributing to the large average speed of the entire population. This subpopulation (n = 10) had particularly fast speeds and average yaw angles smaller than 33° in magnitude, demonstrating that the fastest lipid-coated beads migrated primarily in the parallel orientation (Figure 4B and Table 2).

In addition, lipid-coated ellipsoidal beads displayed greater average trajectory curvature compared with uncoated beads (Figure 4, C and D, and Table 2). Closer examination revealed that a subpopulation of lipid-coated beads (n = 17), which generally corresponded

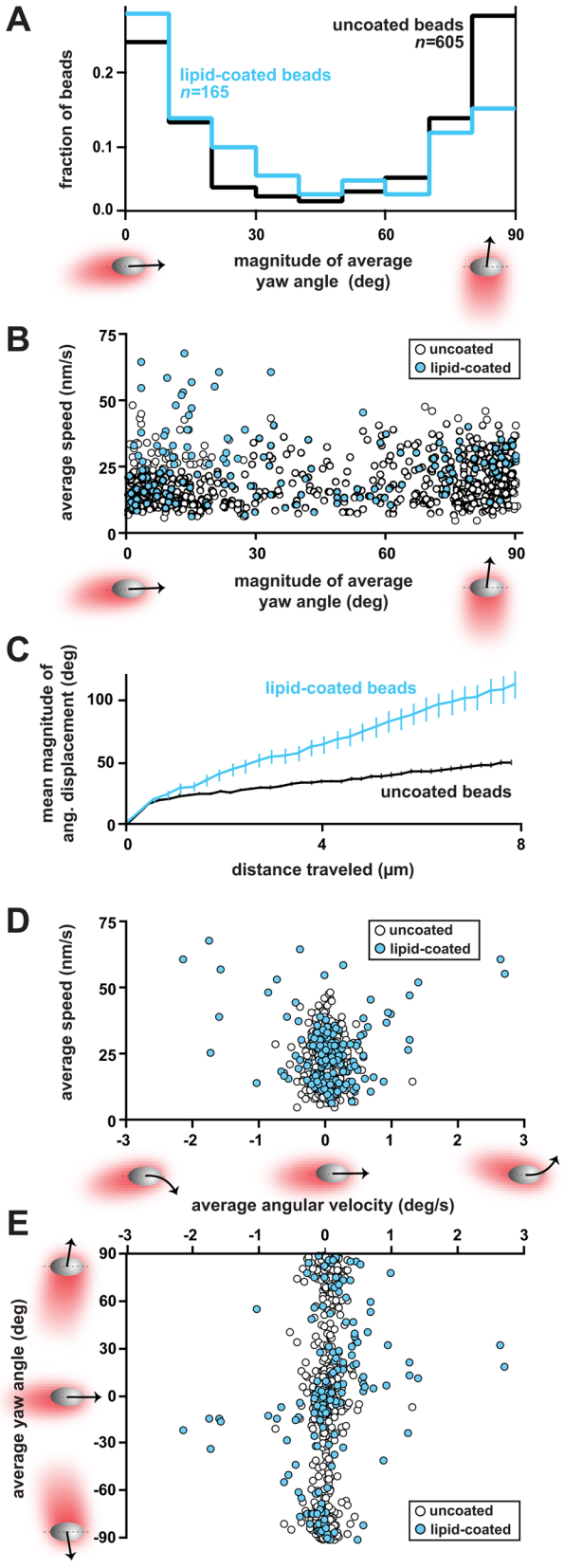

FIGURE 4: Lipid-coated beads with mobile ActA exhibit significant changes in orientation, speed, and angular velocity. (A) The distribution of magnitudes of the average yaw angles of uncoated beads (black line) revealed that the majority of uncoated beads moved in either the parallel orientation (average yaw angle: 0°–30°) or perpendicular orientation (average yaw angle: 60°–90°). These two orientations were approximately equally prevalent in the population of uncoated beads. Lipid-coated beads (cyan line) showed a strong preference to move in the parallel orientation, as opposed to the perpendicular orientation. (B) The speed of beads depended slightly on bead orientation. A modest correlation (Spearman's r = 0.15, $p < 0.05$) between the average speed and average yaw angle was observed for uncoated beads (open circles). Lipid-coated beads (cyan circles) migrated significantly faster (by Wilcoxon rank-sum test, $p < 0.001$; mean of average speed = 25.9 nm/s; SD = 12.5; n = 165) compared with uncoated beads (mean of average speed = 19.9 nm/s; SD = 8.7; n = 605). (C) Lipid-coated beads had increased angular displacements compared with uncoated beads. The mean of the magnitudes of the angular displacement is plotted as a function of distance traveled for each population. Error bars = SEM. (D) On average, most ellipsoidal beads had small average angular velocities during migration. A subpopulation of lipid-coated beads (n = 17) exhibited large average angular velocities greater than 0.8°/s in magnitude. This subpopulation generally corresponded to beads migrating in tight persistent circles and fast speeds. (E) Curving beads with increased angular velocities generally had small yaw angles and were thus oriented close to the parallel orientation. The average yaw angle of each bead is plotted as a function of the average angular velocity.

to the circling individuals readily discerned by eye (see Figure 3C), had remarkably large angular velocities compared with the rest of the population, with magnitudes greater than 0.8°/s (Table 2). As mentioned above, we found only a single bead migrating in this manner in the uncoated population. These circling, lipid-coated beads had a tendency to curve without any obvious preference in turning direction (clockwise vs. counterclockwise trajectory; Figure 4, D and E).

Overall our results demonstrate that ActA polarization due to lateral mobility on a fluid surface has profound effects on motility, such as enhanced speed and increased trajectory curvature. As we show in our simulations (see next section), the experimentally observed differences between lipid-coated and uncoated beads, that is, preference for the parallel orientation and increased circling, are directly predicted properties that emerge from the simple alteration of the actin-attachment sites on the particle surface from being fixed (for uncoated beads) to being laterally mobile (with lipid coating).

Mechanics of a viscoelastic actin network combined with branching of pushing and tethered filaments at the actin–bead interface explain ellipsoidal bead behaviors

Three striking and unexpected features of our observations must be consistent with an accurate biophysical description of actin-based movement. First, movement of ellipsoidal beads is approximately equally stable in either parallel or perpendicular orientations, whereas movement for lipid-coated beads with mobile ActA is more stable in the parallel orientation. Second, movement at intermediate yaw angles is unstable, although orientation switching does occur as a relatively rare event. Third, spontaneous symmetry breaking occurs in the parallel orientation exclusively.

We considered a number of existing theories of actin-based force generation to determine whether any could explain these findings. We found that models of force generation by filament end-tracking proteins (Dickinson and Purich, 2002; Dickinson *et al.*, 2004), by pushing filaments as tethered ratchets (Mogilner and Oster, 1996, 2003; Dickinson and Purich, 2002; Dickinson *et al.*, 2004), or by an elastic gel in the simplest form of the elastic-propulsion model (Gerbal *et al.*, 2000a) cannot independently explain our experimental results. First, when filaments in the comet tail were

	Uncoated beads					
	Mean of average speed (nm/s)	SD	Mean magnitude of average angular velocity (deg/s)	SD	Mean magnitude of average yaw angle (deg)	SD
Spheres (n = 184)	22.0	7.7	N/A	N/A	N/A	N/A
Ellipsoids (n = 605)	19.9	8.7	0.10	0.11	46.9	34.0
Parallel (n = 255)	18.2	8.1	0.10	0.13	9.9	7.5
Perpendicular (n = 287)	21.2	8.8	0.10	0.10	80.1	7.5
			Lipid-coated beads			
Ellipsoids (n = 165)	25.9	12.5	0.33	0.46	38.0	31.1
Parallel (n = 85)	26.5	14.8	0.35	0.52	11.1	8.3
Perpendicular (n = 52)	26.1	6.7	0.20	0.19	78.2	8.4
Fast subpopulation ≥50 nm/s (n = 10)	59.2	5.1	1.37	0.97	14.3	8.9
Circling subpopulation ≥0.8°/s (n = 17)	42.8	16.2	1.46	0.58	26.4	18.4

TABLE 2: Summary of average speed, angular velocity, and yaw angle for uncoated, lipid-coated beads and subpopulations based on motile behavior.

modeled as tethered ratchets growing from a completely rigid tail with branching dynamics, we found that the motile beads stabilized in the perpendicular orientation only (Figure 5A and Video S4). Similar results were obtained when filaments in the comet tail were modeled as ratchets with uniform nucleation along the surface instead of branching dynamics (Video S5). On the other hand, when we used the simple continuous model of a growing elastic actin tail, the beads broke symmetry and moved stably in the parallel orientation only (Figure 5B and Video S6). Using this elastic model, we also simulated a bead that broke symmetry in the perpendicular orientation—a situation that did not occur spontaneously in our experiments—by placing the initial cloud asymmetrically on the side of the bead (Video S7). After initiating movement in the perpendicular orientation, the bead rapidly turned to the parallel orientation without switching back, showing that when beads migrate using only elastic propulsion, the parallel orientation is preferred at steady state regardless of bead orientation during symmetry breaking.

These individual models of actin-based propulsion were incapable of recapitulating ellipsoidal bead migration as observed experimentally. However, we can satisfactorily explain most features of our data with a combination of the tethered-ratchet polymerization theory (Mogilner and Oster, 2003) and the elastic-propulsion model (Gerbal *et al.*, 2000a; our mathematical model in the Supplemental Material). According to both theories, transient attachments of actin filaments from the comet tail to the surface of a moving particle cause an effective drag on the particle, in our case, an ellipsoidal bead. This drag is overcome by a pushing force generated by elastic recoil of bent filaments growing against the surface (Mogilner and Oster, 2003), macroscopic elastic stress of the growing actin network (Bernheim-Groswasser *et al.*, 2005), or more likely, a combination of both mechanisms. Based on our two-dimensional computational mesoscopic model of actin propulsion, which combines elastic-propulsion and actin-filament branching mechanics, the actin meshwork of the comet tail is represented as a node-and-spring viscoelastic network (Figure 5C), similar to a model recently reported (Dayel *et al.*, 2009). The network springs are linear and exert elastic forces. When these springs are stretched beyond a threshold, they break and introduce viscoelastic instead of just elastic actin-tail behavior. Viscoelastic forces are included explicitly in the balance of forces on the surface of the bead, the ellipsoidal geometry of which is also incorporated in the model. In addition to this actin network, individual actin filaments are represented as semirigid rods growing from nodes at the actin tail–bead interface. These filaments impinge on the bead surface and exert active pushing forces resisted by filaments transiently attaching to the surface. Together, these pushing and tethering forces effectively generate reactive viscoelastic stresses in the actin network.

In our simulations, addition of individual dynamic filaments to the interface of the elastic actin gel and the ellipsoidal bead was crucial in allowing the motile bead to become bistable, moving persistently both in parallel and perpendicular orientations, as shown by both simulations and analytical estimates (Figure 5, D and E, Video S8, and our mathematical model in the Supplemental Material). With a specific choice of model parameters, our simulations generated in silico bead movements that mimic the observed in vitro bead behaviors. Specifically, simulated beads initiated motility in the parallel orientation (Figure 5E and Video S8), in agreement with the data (see Figure 2B and Table 2). These particular results differ from a recent report, which showed perpendicular symmetry breaking both in vitro and in silico (Dayel *et al.*, 2009), probably due to differences in the experimental conditions, which are discussed further in our mathematical model (Supplemental Material). Furthermore, our simulations predicted that the diagonal orientation of ellipsoidal beads is unstable, because the average torque, produced by hundreds of pushing and pulling filaments and elastic stresses, goes out of balance, and this balance is restored only when a bead approaches the parallel or perpendicular orientation. This combined viscoelastic-ratchet model also recapitulates the process of switching between parallel and perpendicular orientation in the range of once per tens of minutes, consistent with the overall orientation bistability observed and in semiquantitative agreement with the experimental data (switching rate 1 in ~170 min; see our mathematical model in the Supplemental Material for additional discussion). When we simulated the behavior of migrating ellipsoidal beads and calculated yaw angles, we found that the combined model generated a U-shaped distribution of instantaneous yaw angles, suggestive of the bistability in bead orientation observed in the system (Figure 5D).

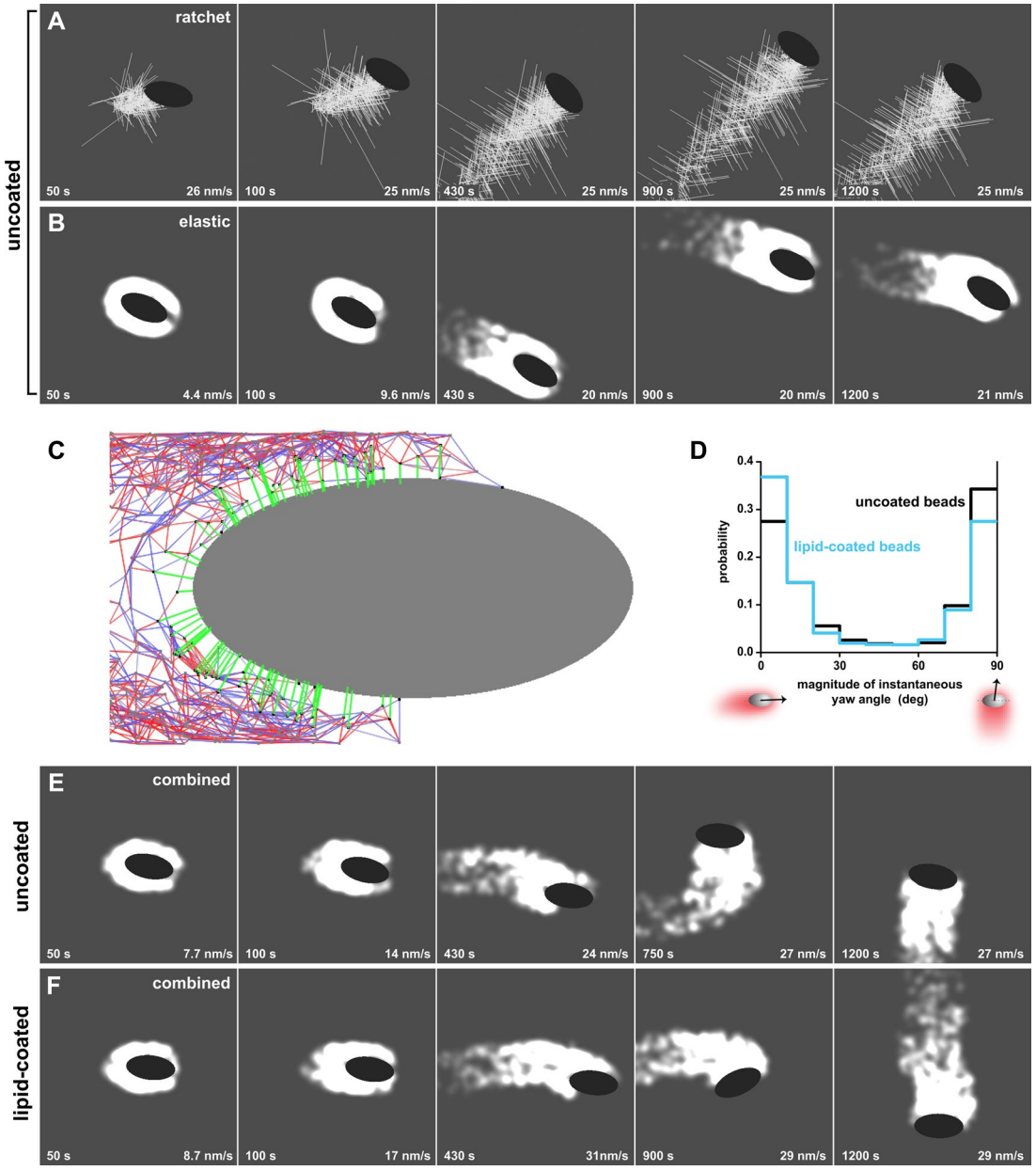

FIGURE 5: A combined viscoelastic-ratchet model of actin polymerization recapitulates the migration of ellipsoidal beads. (A) Snapshots show a simulated ellipsoidal bead being propelled by actin filaments acting as ratchets with autocatalytic branching dynamics. The bead initiates motility in the parallel orientation and rapidly switches to migrating in the perpendicular orientation, where it remains during the length of the simulation. See also Video S4. (B) Simulations of a bead propelled only by a viscoelastic actin tail, without explicit filament ratchets, show that the bead exclusively migrates in the parallel orientation. The tail is illustrated by a continuous actin density so that the shading is proportional to the local number of actin network nodes. A lighter shade corresponds to higher density. See also Video S6. (C) Schematic of the combined viscoelastic-ratchet model depicts a migrating bead (gray) that is pushed by an actin network (red, blue, and green). The actin network is represented by a deformable node-and-spring network, at which growing filaments (green) are anchored. Network springs can be stretched (blue) or compressed (red). The springs break when a certain stretch-force threshold is exceeded. The nodes and springs also disassemble with a constant rate. The barbed end of each newly created filament grows against the bead surface exerting a pushing force, while the pointed end remains anchored at the network. All forces and torques generated by filament pushing and spring deformations are balanced. (D) The combined viscoelastic-ratchet model predicts a U-shaped distribution of instantaneous yaw-angle magnitudes for both uncoated (black line) and lipid-coated (cyan line) beads. The distribution for the lipid-coated beads is slightly skewed toward greater parallel orientation probability. (E) Simulations of an uncoated migrating bead using the combined viscoelastic-ratchet model show that the bead breaks symmetry in the parallel orientation and eventually switches to migrate in the perpendicular orientation (at ~700 s). Note that the time for the fourth frame of this sequence does not correspond to the other panels. See also Video S8. (F) Simulations of a lipid-coated migrating bead using the combined viscoelastic-ratchet model with the same initial condition as in (E) show that the bead breaks symmetry in the parallel orientation and eventually switches to migrate in the perpendicular orientation (at ~900 s). See also Video S9. Time: s. Speed: nm/s.

Using the combined model and our observations of the effects of ActA lateral surface mobility on ellipsoidal bead behavior, we simulated the movement of lipid-coated beads under identical conditions to determine whether this model could also account for the changed behavior resulting from this experimental perturbation. The sole changes to the model were to allow the attachment points (ActA) to be pulled backward by actin filaments when attached and to relieve the tethering forces parallel to the bead surface (see our mathematical model in the Supplemental Material). Simulations showed that beads with laterally mobile ActA broke symmetry and migrated stably in the parallel orientation but were also able to switch orientation (Figure 5F and Video S9). However, these beads stayed in the parallel orientation for a longer time before switching orientation (Figure 5F and Video S9, switches at ~900 s), as compared with uncoated beads (Figure 5E and Video S8, switches at ~700 s). Yaw-angle estimates obtained from simulations of lipid-coated bead movement also generated a U-shaped distribution of instantaneous yaw angles, predicting migration in both the parallel and perpendicular orientations, but with the parallel orientation slightly predominating (Figure 5D). The foregoing simulations were all performed in two dimensions; in the more realistic three-dimensional case, computer simulations of the deforming viscoelastic actin tail become forbiddingly long. Therefore, in three dimensions we simulated a formally rigid actin tail with effective point-like elastic forces, which capture macroscopic elastic effects. Qualitatively, the three-dimensional approximation of the combined viscoelastic-ratchet model gave results similar to those of the two-dimensional model, although the three-dimensional model shows an even greater bias for migration in the parallel orientation by lipid-coated beads, providing an even better fit to the experimental data (see Figure 4A and our mathematical model in the Supplemental Material).

The combined viscoelastic-ratchet model can qualitatively explain the emergence of circling in lipid-coated ellipsoidal beads. On moving lipid-coated beads, surface molecular complexes (ActA) attached to actin filaments are dragged rearward with respect to the bead, as suggested by our experimental observations (see Figure 3A and Giardini *et al.*, 2003). The distribution of pulling forces generated by the tail is therefore expected to be biased toward the rear. The distribution of ActA is, however, more or less symmetric with respect to the long axis of the bead (Figure 3B), so that the pulling forces, having the same symmetry, create no torque. In contrast, the distribution of pushing forces, which is expected to follow the actin distribution, can be biased toward one side, for example, toward the left side of the bead, as shown in Figure 3B. These skewed pushing forces are locally normal to the bead surface and create a significant torque due to the ellipsoidal bead geometry (in which surface normals are not directed toward the bead's center). This torque is in a direction that would cause the lipid-coated bead shown in Figure 3B to rotate counterclockwise, as was observed. We further discuss this effect in our mathematical model (Supplemental Material).

Bead orientation influences speed

Elastic biophysical models predict that shape and local curvature of the bead surface should have an effect on actin polymerization–based force generation that would in turn affect the speed of cargoes (Gerbal *et al.*, 2000a; Noireaux *et al.*, 2000; Bernheim-Groswasser *et al.*, 2005). In the development of the combined viscoelastic-ratchet model, we primarily considered bead orientation, and therefore wondered whether speed could be used as an independent measurement to test the accuracy of the model predictions. To elucidate whether the speed or mode of force generation by the comet tail might be related to the orientation of beads, we measured the speed of uncoated beads as a function of their yaw angles. As a control, we determined the movement of uncoated spherical beads of comparable size (1-μm diameter) and found they moved at speeds similar to those for ellipsoids (Table 2), but ellipsoids had a distinctly slower subpopulation that contributed to their slightly lower average speed (Supplemental Figure S1). Like uncoated ellipsoidal beads, uncoated spherical beads moved in very straight trajectories. For ellipsoidal beads, there was a weak correlation (Spearman's $r = 0.15$, $p < 0.05$) between the average speed and yaw angle over the population, such that beads migrating in the perpendicular orientation were on average slightly faster than beads in the parallel orientation (Table 2) with a statistically significant difference (by Wilcoxon rank-sum test, $p < 0.001$).

When we used the combined viscoelastic-ratchet model to determine the expected speed of beads in each orientation, we found that the speed of beads migrating in the perpendicular orientation was ~24% higher than that of beads in the parallel orientation (see our mathematical model in the Supplemental Material), in good agreement with our experimental data, which shows a 16% increase (Table 2). Notably, Figure 4E and Video S8 demonstrate the increased speed predicted when the simulated ellipsoid approaches or completely switches to the perpendicular orientation. The explanation stems from the force balance: the pulling force is proportional to speed, while the pushing force is a decreasing function of speed (Mogilner, 2006). For beads migrating in the perpendicular orientation, a larger component of the total pushing force propels the bead, whereas in the parallel orientation, only a small component of the pushing force propels the bead, because a significant fraction of the pushing forces *squeeze* the bead and do not contribute to the forward movement (see our mathematical model in the Supplemental Material).

Actin comet tail redistribution on the bead surface precedes changes in bead orientation

An underlying assumption of our theoretical framework has been that net bead movement behavior is caused by the balance of forces and torque exerted by the actin network at the bead surface. The excellent agreement between the steady-state movement data and our combined viscoelastic model suggests that torque generated by changes in the arrangement of the actin comet tail on the surface of moving beads should correlate with changes in their orientation. To test this hypothesis, we directly examined actin distributions on the surfaces of individual beads during events in which beads switched orientation or changed direction in their trajectories. We asked how the orientation switch was related, over time, to the distribution of actin around the bead. As mentioned earlier, spontaneous orientation switching was a rare event for beads migrating at steady state (see Table 1), but these events did reveal noticeable rearrangements of actin in the comet tail on the surface of lipid-coated beads (Figure 6 and Video S10). Similar actin distribution rearrangements were also observed in uncoated beads, but they were less pronounced (unpublished data). As illustrated in Figure 6, a lipid-coated bead's gradual switch from the perpendicular to the parallel orientation was accompanied by a marked increase in actin in the region of the bead that was to become the new back. The increase in actin density at the new back of the bead was followed by the repositioning of the comet tail such that it became roughly centered at the new back.

Since we observed that changes in bead orientation were preceded by actin comet tail rearrangements, we wondered whether these changes in actin distribution could also be involved in changes in motile behavior. To determine this, we analyzed the movement of

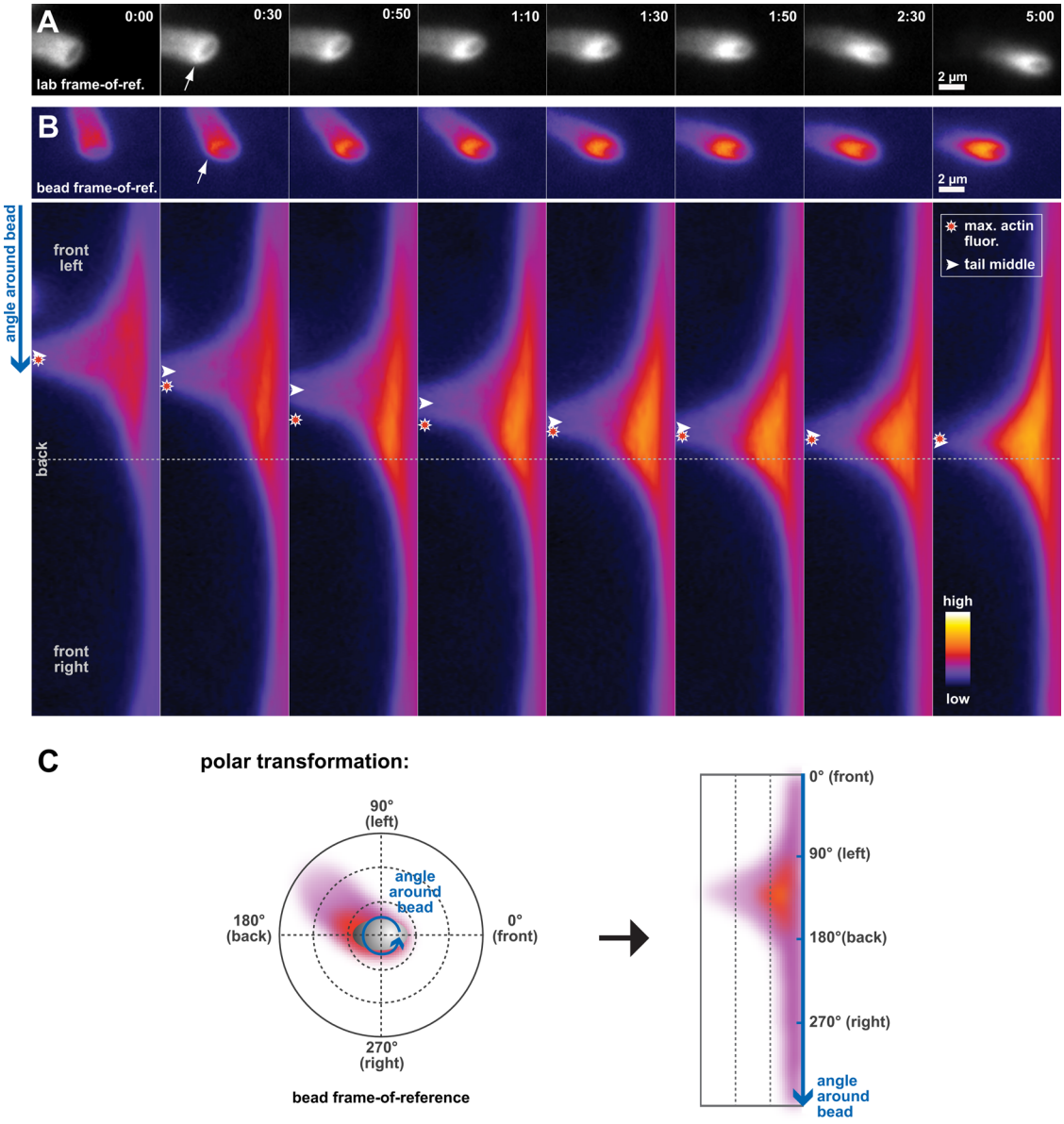

FIGURE 6: Actin redistribution in the comet tail precedes changes in ellipsoidal bead orientation. (A) Fluorescent actin levels were observed to increase at the pole of a lipid-coated bead that became the new back (arrow at 0:30) prior to the bead fully switching from the perpendicular to the parallel orientation. Images are shown in the lab frame of reference. Time: min:s. (B) Time-lapse frames in the bead frame of reference (top), which correspond to the frames shown in panel (A), were used to generate polar-transformation images (bottom). The angular position around the bead is represented as vertical position in the transformed images. Arrowheads indicate the approximate position of the middle of the comet tail. Stars indicate the location of the maximum actin fluorescence measured on the bead surface. Before switching orientation (time = 0:00), the middle of the bead's actin comet tail effectively coincides with the position of the maximum actin fluorescence (overlapping arrowhead and star). While switching orientation, actin accumulates near the prospective back of the bead (see stars; times = 0:30–1:30) before the entire tail shifts position and follows the direction of the initial actin redistribution. Eventually, the bead completely switches to the parallel orientation, as the middle of the comet tail and the maximum actin fluorescence go back to spatially coincide (times = 1:50–5:00). Images were pseudocolored in ImageJ (Fire lookup table). Scale bar: 2 μm. Time: min:s. See also Video S10. (C) The schematic illustrates the overall approach used in the polar transformation of images. Images in the bead frame of reference are processed so that the angle around the centroid of the bead becomes the *y*-axis (blue arrow) of polar-transformed images.

an uncoated bead that changed direction multiple times during its trajectory. The particular bead shown in Figure 7 started off migrating for ~2 min in a counterclockwise trajectory, changed to migrating clockwise for ~3 min, and ended by describing a counterclockwise loop. As the angular velocity of the bead alternated from positive to negative and back to positive, the position with the highest level of actin on the bead's surface also alternated and correlated with changes in bead direction (Figure 7B). During these changes in direction, increased actin density was found on the surface of the bead corresponding to the inside of the curve, and the

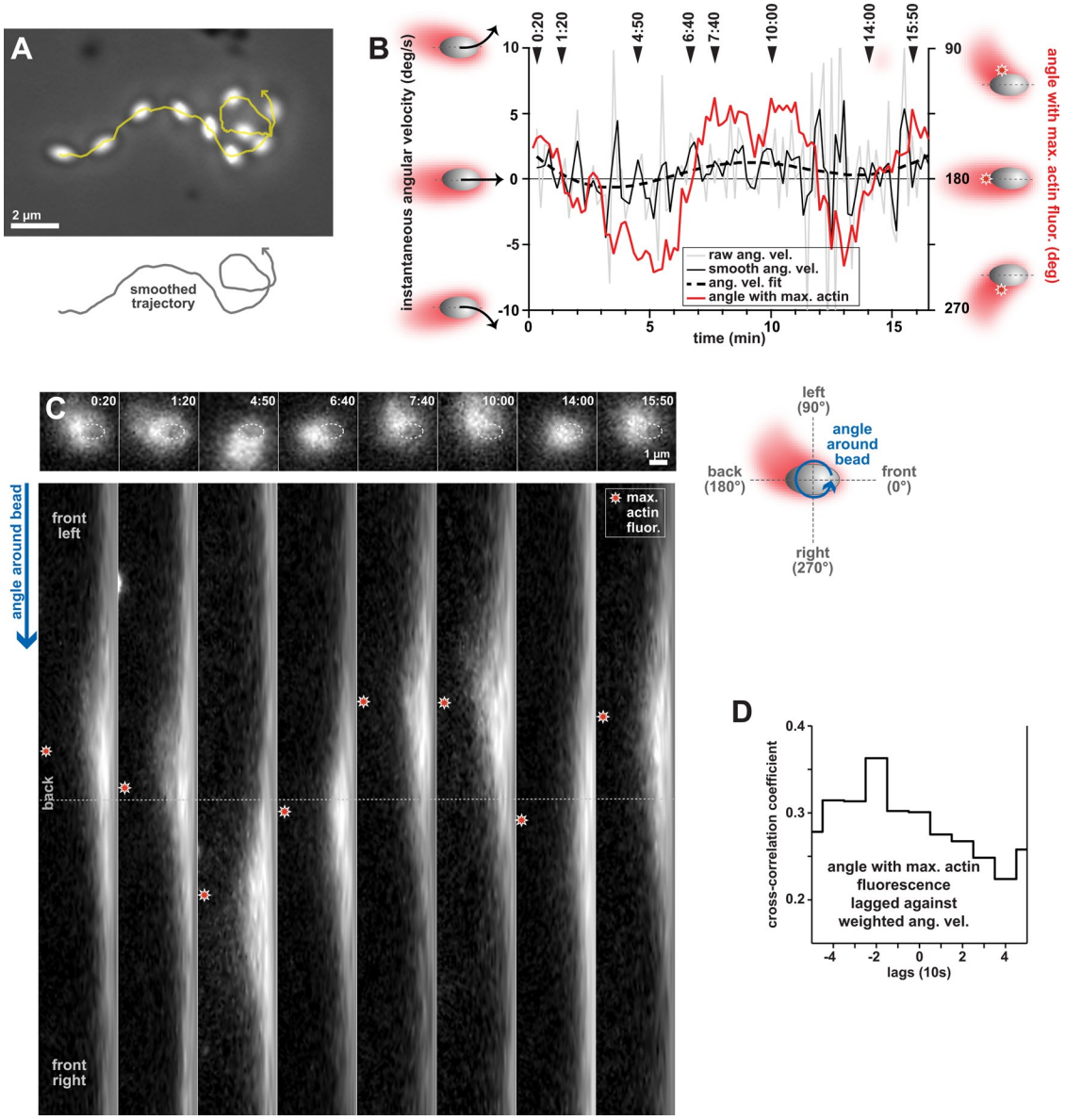

FIGURE 7: The actin comet tail alternates position from side to side as an ellipsoidal bead changes direction in its trajectory. (A) Phase-contrast images from multiple frames of a time-lapse sequence are composited to show the location of an uncoated bead that changes direction along its trajectory. The raw trajectory is shown in yellow and the arrowhead indicates that the bead moved from left to right. A smoothed version of the track is shown below the image to clarify the direction of the final loop. Scale bar: 2 μm. (B) The instantaneous angular velocity (left *y*-axis) and angular position of the maximum actin fluorescence on the bead surface (right *y*-axis) correlate with each other as the bead changes direction. The raw instantaneous angular velocity of the bead (gray line) was smoothed using a weighted average (black solid line) and fit using a polynomial function (dashed black line). The left *y*-axis of the graph was truncated at –10°/s and 10°/s so that five values greater than 10°/s in magnitude are not shown. The angular position of the maximum actin fluorescence on the bead surface (right *y*-axis, red line) is used to follow the location of the comet tail. The time points indicated at the top of the graph correspond to the images in (C). (C) The actin comet tail slides about the back of the bead from one side to the other as the bead changes direction. Time-lapse images in the bead frame of reference (top) generated the polar-transformation images (bottom). The location of the bead is depicted by the outline (top, dashed white ellipses). The angle around the bead is represented vertically in the transformed images. Stars indicate the location of the maximum actin fluorescence measured on the bead surface. Images shown correspond to time points indicated in the graph in (B). The schematic on the right illustrates the polar transformation. Scale bar: 1 μm. Time: min:s. See also Video S11. (D) The time-lagged cross-correlation of the angular position of the maximum actin fluorescence on the bead and the weighted angular velocity shows a peak at a time lag of –2 (or –20 s). Changes in the direction of bead trajectory turning (angular velocity) preceded the repositioning of the comet tail on the bead's surface by ~20 s.

actin tail appeared to slide about the back of the bead from one side to the other (Figure 7, B and C, and Video S11). Interestingly, the time-lagged cross-correlation of the smoothed version of angular velocity with the position of the maximum actin intensity showed that changes in the direction of a bead's trajectory preceded (by ~20 s) rearrangements in the placement of the actin comet tail on

the bead's surface (Figure 7D). In addition, the speed of this bead appeared to vary contemporaneously with angular velocity (unpublished data). Thus changes in bead speed appeared to also precede rearrangements of actin in the comet tail. Additional cross-correlation analysis revealed that rearrangements of actin in the comet tail near the surface of this bead preceded (by at least 10 s) changes in orientation as measured by its yaw angle (unpublished data), similar to what was observed for the bead in Figure 6. To summarize, our data shows that while changes in bead orientation are downstream effects of changes in comet tail distribution on the bead surface, bead movement (speed and angular velocity) may be a causal predecessor of changes in actin distribution during bead migration. We propose that perturbations to bead movement, in combination with subsequent rearrangements of the comet tail on the surface of the bead, generate the torque necessary to ultimately change the orientation of the bead during migration. In our mathematical model (Supplemental Material), we discuss how the temporal sequence of changes in motion, bead orientation, and actin density can be understood from the modeling point of view.

DISCUSSION

Based on the original elastic model of bacterial actin-based propulsion, actin gel growth should generate significant squeezing forces on curved surfaces, such as the back of a bacterium, propelling the bacterium forward (Gerbal *et al.*, 2000a). Such squeezing forces have been demonstrated on deformable lipid vesicles and oil droplets, which become compressed to a teardrop shape (Giardini *et al.*, 2003; Upadhyaya *et al.*, 2003; Boukellal *et al.*, 2004). According to the elastic-propulsion model, both rod-shaped bacteria and ellipsoidal beads are predicted to move most stably in the direction parallel to their long axes, because most of the squeezing occurs at the sides, generating a torque that aligns the long axis of the particle with that of the actin tail. In contrast, the tethered-ratchet model with specific parameters and assumptions (see our mathematical model in the Supplemental Material), predicts that ellipsoidal beads should move in the perpendicular orientation, because the bead in a skewed orientation experiences a net force pushing the bead forward not only parallel to the long axis of the comet tail, but also perpendicular to it. The direction of this perpendicular push is such that the bead's lagging pole rotates away from the long axis of the tail. This rotation causes the lagging pole to effectively lose actin filaments, while the leading pole gets exposed to nascent filaments. As a result, the actin network spreads down the long side of the bead surface, keeping the bead in the perpendicular orientation. Instead of the scenarios predicted by the elastic-propulsion and tethered-ratchet models, we found experimentally that ellipsoidal beads had no preference for either orientation during steady-state motility. The combination of actin network elasticity and filament ratcheting with branching dynamics into a mesoscopic model was necessary to explain our experimental results. Our combined model predicts that beads that migrate in the parallel orientation experience a torque generated by elastic actin squeezing, which dominates and aligns the bead with the actin tail's long axis. When beads migrate in the perpendicular orientation, squeezing is weaker, and the geometric and kinetic effects of the branching actin filaments in the network dominate. Strikingly, the elastic squeezing effect and actin-filament pushing and spreading combine in such a way that the overall stability of movement is very similar for the two orientations, and the population of beads distributes itself almost evenly between them. Preliminary simulations showed that the qualitative result of the model—the bistability of bead orientation—is robust when the model's parameters are varied, but the predicted fraction of beads in each orientation is a function of the parameter values. Our combined model could be applicable to other important protrusive phenomena as discussed in our mathematical model (Supplemental Material).

Because the actin-based motility of actual bacteria is almost exclusively parallel to their long axis, it is likely that the polar distribution of bacterial proteins that initiate motility is more important than their shape for determining their orientation during migration. In fact, *Escherichia coli* bacteria expressing the *S. flexneri* IcsA/VirG proteins exhibited a much shallower gradient of protein polarization than wild-type *S. flexneri* (Robbins *et al.*, 2001) and occasionally migrated perpendicular to their long axes (Goldberg and Theriot, 1995) in a manner similar to our ellipsoidal beads uniformly coated with ActA. For normal *L. monocytogenes*, polarization of ActA is a direct consequence of the pattern of cell wall growth (Rafelski and Theriot, 2006), enforcing persistent unidirectional movement parallel to the bacterial long axis.

Although *L. monocytogenes* is similar in shape to the ellipsoidal beads used in this study, it is important to note that differences in the localization of the ActA protein in these two systems have significant impact on biophysical motile parameters. *L. monocytogenes* expresses ActA in a polarized manner, while the surfaces of ellipsoidal beads were coated uniformly with ActA. When we bound ActA protein to a fluid lipid layer coating the surface of ellipsoidal beads and thus allowed ActA to freely move, ActA became polar and colocalized with the actin comet tail, as observed previously for spherical beads (Giardini *et al.*, 2003). This lateral mobility and consequent polar ActA distribution allowed ellipsoidal beads to recapitulate the predominant orientation and curved trajectories, such as tight circles, commonly observed in wild-type, migrating *L. monocytogenes*. Thus the polarization of ActA in *L. monocytogenes* is probably crucial not only for its characteristic orientation but also for the complex motile behaviors in which it engages.

Since ActA is the only bacterial factor necessary for the actin-based motility of artificial particles, this protein likely represents the site of actin-filament attachment to the surface of beads, either directly by binding or indirectly through interactions with cytoplasmic proteins, such as Enabled/vasodilator-stimulated phosphoprotein (Ena/VASP) family members or the Arp2/3 complex, which are proteins known to bind directly to actin filaments (Pistor *et al.*, 1995; Gertler *et al.*, 1996; Mullins *et al.*, 1997; Huttelmaier *et al.*, 1999; Zalevsky *et al.*, 2001). When mobile ActA becomes clustered on the back of lipid-coated ellipsoidal beads, the distribution of pulling filaments attached to ActA—and thus attached to the bead—could become significantly biased, creating a rearward force applied at the back of the bead that generates torque, rotating beads toward the parallel orientation. The computational simulations revealed that behavioral features of lipid-coated beads compared with uncoated beads—preference for the parallel orientation and increased circling—can arise from the simple introduction of lateral mobility of attachment points on the particle surface without any other changes in model parameters.

Specific mutations in the ActA protein or in binding partners that alter their biochemical activities and interactions have been shown to cause changes in large-scale behavior strongly reminiscent of several of our observations. For example, mutation of Ena/VASP-binding domains in ActA or deletion of the F-actin–binding domain in Ena/VASP can cause *L. monocytogenes* to move in small tight circles (Auerbuch *et al.*, 2003) similar to the extreme curved patterns of lipid-coated ellipsoids (see Figure 3). Even more strikingly, a cluster of charged-to-alanine mutations in a region of ActA with unknown function generates a bacterial strain that can "skid" and move sideways (perpendicular to the long axis) in host cells (Lauer

et al., 2001). These behavioral changes are not due to changes in the degree of polarization of the ActA protein on the bacterial surface, as protein polarization in the mutant is indistinguishable from that of the wild-type (Rafelski, 2005). Instead, the large-scale behavioral changes arising from these mutations are likely to be due to modest changes in affinity, binding kinetics, or biochemical activity for surface-associated proteins. Because we are able to phenocopy these biochemical alterations with purely physical changes in protein distribution or lateral mobility in ellipsoidal beads, these comparisons open a window for exploring the connections between protein–protein interactions at the molecular scale and large-scale cooperative emergent behaviors of whole motile systems.

The propulsion of cargo, such as bacteria, vesicles, and artificial beads, by polymerizing networks of actin filaments represents an attractive and widely used model system for actin-based motility amenable to both biochemical and biophysical dissection. In this study, we characterized several unexpected large-scale changes in movement caused by simple physical alterations of the underlying cargo: deformation of spherical beads into ellipsoidal shapes and enhancement of lateral mobility for attachment points of actin filaments to the cargo. These physical changes phenocopy several previously described mutant behaviors of motile bacteria. By incorporating realistic geometries and combining existing biophysical models of actin force generation, we are able to explain most quantitative features of our data, further confirming the broad explanatory power of this hybrid physical model. These findings illustrate some of the ways that large-scale complex changes in behavior can emerge cooperatively from alterations in molecular functions.

MATERIALS AND METHODS

Preparation of ellipsoidal beads

Ellipsoidal beads were prepared as previously described (Lu *et al.*, 2001). Briefly, 1-µm carboxylated polystyrene microspheres (Polysciences, Warrington, PA) were placed in a viscoelastic matrix (6% polyvinyl alcohol), heated to ~200°C in a box oven, and stretched uniaxially. The film containing the beads was cooled and dissolved using an isopropanol/water mixture to recover the beads before functionalizing their surfaces with carboxylate. Electron microscopy revealed that the beads used in this study had average dimensions of 1.8 µm × 0.8 µm (length, SD = 0.3; width, SD = 0.2; n = 30), with an average aspect ratio of 2.2.

For coating beads with a lipid bilayer, a 50:1 ratio of carboxylated ellipsoidal beads were mixed with unilamellar vesicles (lipid composition consisted of a 46:50:2:2 M ratio of phosphatidylcholine:cholesterol:fluorescein-phosphatidylethanolamine:Ni-nitrolotriacetic acid chelating lipid) and prepared as previously described (Hope *et al.*, 1985; Linseisen *et al.*, 1997; Giardini *et al.*, 2003). All phospholipids were obtained from Avanti Polar Lipids (Alabaster, AL). His-tagged ActA was purified as previously described (Welch *et al.*, 1998; Cameron *et al.*, 1999) and adsorbed on the surface of uncoated or lipid-coated beads at saturating amounts (Giardini *et al.*, 2003). For direct visualization of ActA, cysteine-modified ActA (Upadhyaya *et al.*, 2003) was labeled with fluorescein-5-maleimide (Invitrogen, Carlsbad, CA) using the manufacturer's protocol. Briefly, 10 µM ActA-cysteine was incubated with 0.2 mM fluorescein-5-maleimide for 1 h at room temperature in phosphate buffered saline (137 mM NaCl, 2.7 mM KCl, 8.03 mM Na_2HPO_4, 1.47 mM KH_2PO_4). The fluorescein-ActA was then purified by dialysis and gel filtration.

Bead motility assays

Motility assays in this study were adapted from previous work (Cameron *et al.*, 1999). Slides were prepared by adding ActA-coated or ActA-lipid-coated beads to *X. laevis* egg cytoplasmic extract, which was diluted to 40% of the original protein concentration (using *Xenopus* extract buffer; Murray, 1991) and supplemented with trace amounts of tetramethylrhodamine iodoacetamide–labeled monomeric actin and an ATP-regenerating mix (Murray, 1991). The slide chamber depth was restricted using 2-µm silica spherical beads. Bead motility was visualized on a Zeiss Axioplan microscope (Jena, Germany) equipped with phase-contrast and epifluorescence optics and a CCD camera (MicroMax 512 BFT; Princeton Instruments, Trenton, NJ). Phase-contrast and fluorescence images were acquired every 10 s for 100 frames for most time-lapse sequences using MetaMorph software (Molecular Devices, Sunnyvale, CA). All time-lapse sequences taken during steady-state bead motility were acquired between 2 and 4 h after preparing the slide. For the uncoated and lipid-coated ellipsoidal bead populations, a total of 113 and 50 time-lapse sequences were analyzed, respectively. These sequences generated a total number of 605 (50,426 data points) and 165 (12,651 data points) bead trajectories at steady state for uncoated and lipid-coated ellipsoids, respectively. Stationary beads with actin clouds and beads undergoing Brownian motion or symmetry breaking were excluded from our analysis of steady-state movement, as were any track segments during which beads underwent collisions.

Bead movement and fluorescence analysis

Bead positions and orientations were computed from phase-contrast images and assembled into tracks essentially as previously described (Soo and Theriot, 2005b). Trajectories with fewer than 40 data points and track segments during which beads physically interacted with neighboring beads were excluded from the data set, as were cloud-associated beads undergoing Brownian motion. Image sequences in transformed coordinates (bead frame of reference and polar) with linear interpolation were generated using custom plugins to ImageJ (http://rsb.info.nih.gov/ij).

For ellipsoidal beads, yaw was defined as the angle between the average orientation of the long axis of a bead in two consecutive time-lapse frames and the vector describing the bead's movement between those frames (for a simplified diagram, see Figure 2C). Yaw angles were constrained to range between –90° and 90°. Instantaneous speed values were calculated by dividing the straight-line displacement of the centroids of tracked beads by the time elapsed (10 s) between consecutive frames of a time-lapse sequence. The mean of the time-averaged instantaneous speed of each bead (mean of average speed) was usually reported for each population. Instantaneous angular velocities were calculated by dividing the angle between consecutive vectors describing the bead's trajectory by the elapsed time (10 s). The mean of the magnitudes of the time-averaged instantaneous angular velocities of beads (mean magnitude of average angular velocity) was reported for each population (Table 2).

For the time course of tail formation, slides were prepared at time zero and images were collected at each of the designated times over a 5-h period. For each time point, 50 phase-contrast and fluorescence images were acquired across each slide using a 10 × 5 grid. The numbers of beads with comet tails generally parallel, perpendicular, or diagonal to the long axis were counted. Each data point consisted of between 38 and 576 counted beads.

The maximum actin fluorescence on the comet tail was calculated by using polar-transformed images obtained from images in the bead frame of reference and centered on the bead. The fluorescence intensity was averaged in each of 512 regions of 1 pixel × 20 pixels (corresponding to 0.7° × ~2 µm) along the angle coordinate. The position of the region with the largest average fluorescence value

was then reported in degrees and reflected an angle around the bead. Time-lagged cross-correlations were performed using the TSTOOL interface in Matlab software (MathWorks, Natick, MA). Smoothing of the instantaneous angular velocity values was generated in GraphPad Prism software (La Jolla, CA) using a weighted average of five nearest neighbors based on the method of Savitsky and Golay (1964) using a cubic equation. The angular velocity fit-in was generated using a seventh-order polynomial function.

Mathematical modeling of ellipsoidal bead migration

We simulated stochastic coupled dynamics of two populations of actin filaments (attached and detached) at the surface of ellipsoidal beads, calculated the forces and torques exerted by the filaments on the beads, and computed the beads' movements according to the zero total force and torque requirements as described in our mathematical model (Supplemental Material). Simulations were performed on a desktop computer; the code, written in C, is available upon request.

ACKNOWLEDGMENTS

We thank Jennifer R. Robbins for assisting with the advancement of this project at a crucial stage and Susanne M. Rafelski and Karine A. Gibbs for critically reading this manuscript. We particularly thank Adriana T. Dawes for her careful evaluation of an early manuscript, especially the treatment of the mathematical model. This work was supported by National Institutes of Health (NIH–National Institute of Allergy and Infectious Diseases) grant R01-AI36929 to J.A.T. M.A.T. was supported by NIH grant T32GM007276, and J.Z. and A.M. were supported by a NIH Glue grant to the Cell Migration Consortium (National Institute of General Medical Sciences U54-GM64346) and National Science Foundation grant DMS-0315782.

REFERENCES

Auerbuch V, Loureiro JJ, Gertler FB, Theriot JA, Portnoy DA (2003). Ena/VASP proteins contribute to *Listeria monocytogenes* pathogenesis by controlling temporal and spatial persistence of bacterial actin-based motility. Mol Microbiol 49, 1361–1375.

Bernardini ML, Mounier J, d'Hauteville H, Coquis-Rondon M, Sansonetti PJ (1989). Identification of icsA, a plasmid locus of *Shigella flexneri* that governs bacterial intra- and intercellular spread through interaction with F-actin. Proc Natl Acad Sci USA 86, 3867–3871.

Bernheim-Groswasser A, Prost J, Sykes C (2005). Mechanism of actin-based motility: a dynamic state diagram. Biophys J 89, 1411–1419.

Bernheim-Groswasser A, Wiesner S, Golsteyn RM, Carlier MF, Sykes C (2002). The dynamics of actin-based motility depend on surface parameters. Nature 417, 308–311.

Boukellal H, Campas O, Joanny JF, Prost J, Sykes C (2004). Soft *Listeria*: actin-based propulsion of liquid drops. Phys Rev E Stat Nonlin Soft Matter Phys 69, 061906.

Cameron LA, Footer MJ, van Oudenaarden A, Theriot JA (1999). Motility of ActA protein-coated microspheres driven by actin polymerization. Proc Natl Acad Sci USA 96, 4908–4913.

Cameron LA, Robbins JR, Footer MJ, Theriot JA (2004). Biophysical parameters influence actin-based movement, trajectory, and initiation in a cell-free system. Mol Biol Cell 15, 2312–2323.

Cameron LA, Svitkina TM, Vignjevic D, Theriot JA, Borisy GG (2001). Dendritic organization of actin comet tails. Curr Biol 11, 130–135.

Cudmore S, Cossart P, Griffiths G, Way M (1995). Actin-based motility of vaccinia virus. Nature 378, 636–638.

Dayel MJ, Akin O, Landeryou M, Risca V, Mogilner A, Mullins RD (2009). In silico reconstitution of actin-based symmetry breaking and motility. PLoS Biol 7, e1000201.

Delatour V, Helfer E, Didry D, Le KH, Gaucher JF, Carlier MF, Romet-Lemonne G (2008). Arp2/3 controls the motile behavior of N-WASP-functionalized GUVs and modulates N-WASP surface distribution by mediating transient links with actin filaments. Biophys J 94, 4890–4905.

Dickinson RB, Caro L, Purich DL (2004). Force generation by cytoskeletal filament end-tracking proteins. Biophys J 87, 2838–2854.

Dickinson RB, Purich DL (2002). Clamped-filament elongation model for actin-based motors. Biophys J 82, 605–617.

Gerbal F, Chaikin P, Rabin Y, Prost J (2000a). An elastic analysis of *Listeria monocytogenes* propulsion. Biophys J 79, 2259–2275.

Gerbal F, Laurent V, Ott A, Carlier MF, Chaikin P, Prost J (2000b). Measurement of the elasticity of the actin tail of *Listeria monocytogenes*. Eur Biophys J 29, 134–140.

Gertler FB, Niebuhr K, Reinhard M, Wehland J, Soriano P (1996). Mena, a relative of VASP and Drosophila Enabled, is implicated in the control of microfilament dynamics. Cell 87, 227–239.

Giardini PA, Fletcher DA, Theriot JA (2003). Compression forces generated by actin comet tails on lipid vesicles. Proc Natl Acad Sci USA 100, 6493–6498.

Goldberg MB, Barzu O, Parsot C, Sansonetti PJ (1993). Unipolar localization and ATPase activity of IcsA, a *Shigella flexneri* protein involved in intracellular movement. J Bacteriol 175, 2189–2196.

Goldberg MB, Theriot JA (1995). *Shigella flexneri* surface protein IcsA is sufficient to direct actin-based motility. Proc Natl Acad Sci USA 92, 6572–6576.

Gouin E, Gantelet H, Egile C, Lasa I, Ohayon H, Villiers V, Gounon P, Sansonetti PJ, Cossart P (1999). A comparative study of the actin-based motilities of the pathogenic bacteria *Listeria monocytogenes*, *Shigella flexneri* and *Rickettsia conorii*. J Cell Sci 112, 1697–1708.

Gouin E, Welch MD, Cossart P (2005). Actin-based motility of intracellular pathogens. Curr Opin Microbiol 8, 35–45.

Hope MJ, Bally MB, Webb G, Cullis PR (1985). Production of large unilamellar vesicles by a rapid extrusion procedure: characterization of size distribution, trapped volume and ability to maintain a membrane potential. Biochim Biophys Acta 812, 55–65.

Huttelmaier S, Harbeck B, Steffens O, Messerschmidt T, Illenberger S, Jockusch BM (1999). Characterization of the actin binding properties of the vasodilator-stimulated phosphoprotein VASP. FEBS Lett 451, 68–74.

Kocks C, Hellio R, Gounon P, Ohayon H, Cossart P (1993). Polarized distribution of *Listeria monocytogenes* surface protein ActA at the site of directional actin assembly. J Cell Sci 105, 699–710.

Kocks C, Marchand JB, Gouin E, d'Hauteville H, Sansonetti PJ, Carlier MF, Cossart P (1995). The unrelated surface proteins ActA of *Listeria monocytogenes* and IcsA of *Shigella flexneri* are sufficient to confer actin-based motility on *Listeria innocua* and *Escherichia coli* respectively. Mol Microbiol 18, 413–423.

Lauer P, Theriot JA, Skoble J, Welch MD, Portnoy DA (2001). Systematic mutational analysis of the amino-terminal domain of the *Listeria monocytogenes* ActA protein reveals novel functions in actin-based motility. Mol Microbiol 42, 1163–1177.

Linseisen FM, Hetzer M, Brumm T, Bayerl TM (1997). Differences in the physical properties of lipid monolayers and bilayers on a spherical solid support. Biophys J 72, 1659–1667.

Loisel TP, Boujemaa R, Pantaloni D, Carlier MF (1999). Reconstitution of actin-based motility of *Listeria* and *Shigella* using pure proteins. Nature 401, 613–616.

Lu Y, Yin Y, Xia Y (2001). Preparation and characterization of micrometer-sized "egg shells." Adv Mater 13, 271–274.

Mogilner A (2006). On the edge: modeling protrusion. Curr Opin Cell Biol 18, 32–39.

Mogilner A, Oster G (1996). Cell motility driven by actin polymerization. Biophys J 71, 3030–3045.

Mogilner A, Oster G (2003). Force generation by actin polymerization II: the elastic ratchet and tethered filaments. Biophys J 84, 1591–1605.

Mullins RD, Heuser JA, Pollard TD (1998). The interaction of Arp2/3 complex with actin: nucleation, high affinity pointed end capping, and formation of branching networks of filaments. Proc Natl Acad Sci USA 95, 6181–6186.

Mullins RD, Stafford WF, Pollard TD (1997). Structure, subunit topology, and actin-binding activity of the Arp2/3 complex from *Acanthamoeba*. J Cell Biol 136, 331–343.

Murray AW (1991). Cell cycle extracts. Methods Cell Biol 36, 581–605.

Noireaux V, Golsteyn RM, Friederich E, Prost J, Antony C, Louvard D, Sykes C (2000). Growing an actin gel on spherical surfaces. Biophys J 78, 1643–1654.

Peskin CS, Odell GM, Oster GF (1993). Cellular motions and thermal fluctuations: the Brownian ratchet. Biophys J 65, 316–324.

Pistor S, Chakraborty T, Walter U, Wehland J (1995). The bacterial actin nucleator protein ActA of *Listeria monocytogenes* contains

multiple binding sites for host microfilament proteins. Curr Biol 5, 517–525.
Rafelski SM (2005). Integrating Bacterial Polarity with Host-Cytoskeletal Dynamics: Initiation of *Listeria monocytogenes* Actin-Based Motility, Stanford, CA: Stanford University.
Rafelski SM, Theriot JA (2006). Mechanism of polarization of *Listeria monocytogenes* surface protein ActA. Mol Microbiol 59, 1262–1279.
Robbins JR, Monack D, McCallum SJ, Vegas A, Pham E, Goldberg MB, Theriot JA (2001). The making of a gradient: IcsA (VirG) polarity in *Shigella flexneri*. Mol Microbiol 41, 861–872.
Savitzky A, Golay MJE (1964). Smoothing and differentiation of data by simplified least squares procedures. Anal Chem 36, 1627–1639.
Schwartz IM, Ehrenberg M, Bindschadler M, McGrath JL (2004). The role of substrate curvature in actin-based pushing forces. Curr Biol 14, 1094–1098.
Shenoy VB, Tambe DT, Prasad A, Theriot JA (2007). A kinematic description of the trajectories of *Listeria monocytogenes* propelled by actin comet tails. Proc Natl Acad Sci USA 104, 8229–8234.
Smith GA, Portnoy DA, Theriot JA (1995). Asymmetric distribution of the *Listeria monocytogenes* ActA protein is required and sufficient to direct actin-based motility. Mol Microbiol 17, 945–951.
Soo FS, Theriot JA (2005a). Adhesion controls bacterial actin polymerization-based movement. Proc Natl Acad Sci USA 102, 16233–16238.
Soo FS, Theriot JA (2005b). Large-scale quantitative analysis of sources of variation in the actin polymerization-based movement of *Listeria monocytogenes*. Biophys J 89, 703–723.
Tilney LG, Portnoy DA (1989). Actin filaments and the growth, movement, and spread of the intracellular bacterial parasite, *Listeria monocytogenes*. J Cell Biol 109, 1597–1608.
Trichet L, Campas O, Sykes C, Plastino J (2007). VASP governs actin dynamics by modulating filament anchoring. Biophys J 92, 1081–1089.
Upadhyaya A, Chabot JR, Andreeva A, Samadani A, van Oudenaarden A (2003). Probing polymerization forces by using actin-propelled lipid vesicles. Proc Natl Acad Sci USA 100, 4521–4526.
Welch MD, Iwamatsu A, Mitchison TJ (1997). Actin polymerization is induced by Arp2/3 protein complex at the surface of *Listeria monocytogenes*. Nature 385, 265–269.
Welch MD, Rosenblatt J, Skoble J, Portnoy DA, Mitchison TJ (1998). Interaction of human Arp2/3 complex and the *Listeria monocytogenes* ActA protein in actin filament nucleation. Science 281, 105–108.
Zalevsky J, Grigorova I, Mullins RD (2001). Activation of the Arp2/3 complex by the *Listeria* ActA proteinActA binds two actin monomers and three subunits of the Arp2/3 complex. J Biol Chem 276, 3468–3475.

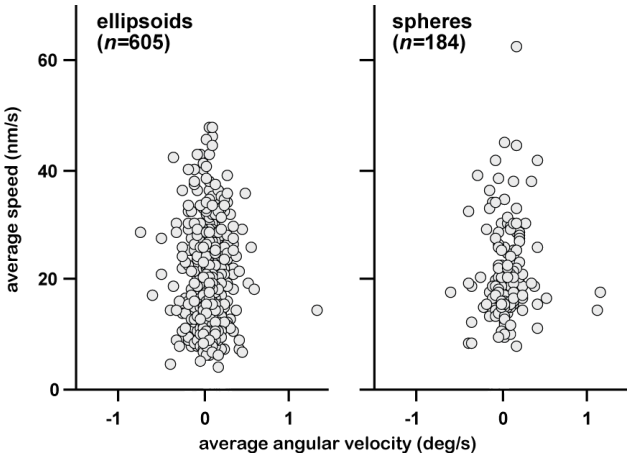

Supporting Figure S1. Spherical and ellipsoidal beads have similar motile behaviors. Spheres with an average diameter of 1 μm and ellipsoids with average dimensions of 1.8 x 0.8 μm have a similar speeds: mean of average speed = 19.9 nm/s, SD=8.7, n=605 for ellipsoids (left); 22.0 nm/s, SD=7.7, n=184 for spheres (right). In general, all of these uncoated beads tend to have relatively straight trajectories, as reflected by the mean of the magnitudes of average angular velocities: 0.10 deg/s, SD=0.11, for ellipsoids (left); 0.12 deg/s, SD=0.15 for spheres (right).

Supporting Text: Mathematical Model

We model ellipsoidal bead propulsion computationally in both 2D and 3D. In 2D, we simulate the combined viscoelastic-ratchet model. But in the more geometrically realistic 3D case, computer simulations of a deforming viscoelastic actin tail become forbiddingly long. Therefore, we treat the actin tail as rigid in 3D but with effective point-like elastic forces on the side to capture macroscopic elastic effects. Qualitative agreement of the results of these two models supports our conclusions.

I. 3D tethered ratchet model with elastic forces concentrated at the tail's edges

Model

A. Geometry

In 3D, the bead is represented as an ellipsoid with two identical short axes being 0.5 μm and a long axis being 1 μm. We define the bead's local coordinate system (*x, y, z*) so that the *x*- and *y*-axes pass through the bead's short axes and the *z*-axis passes through the bead's long axis. The geometry of the bead can be described as

$$\frac{x^2 + y^2}{0.5^2} + \frac{z^2}{1^2} = 1 . \qquad \text{[Eq.1]}$$

We assume that the ActA sites are randomly distributed on the surface of the bead without any spatial bias, and that the actin tail is formed only behind the rear-half of the bead surface that is opposite to the direction of bead movement, because small nascent filaments that are 'in the bead's way' are swept aside and not incorporated into the tail. We also define the tail's frame-of-reference (*X, Y, Z*) which is centered at the bead's centroid but with the *Z*-axis always being parallel to the bead's motion (**Fig. i**). In the tail's frame-of-reference, the immediate comet tail behind the bead is always along the *Z*-axis. We define the orientation of the bead in the tail frame as (θ, φ), where the yaw angle θ is the polar angle between the bead's long axis (*z*-axis) and the tail axis (*Z*-axis), and φ is the azimuthal angle of the bead's long axis about the *Z*-axis in the tail frame. We also define ψ as the rotation of the bead about its long axis. Then, the coordinates of the bead surface in the tail frame-of-reference, $\vec{r}$, can be obtained from the inverse of following Euler rotations:

$$\vec{r}_{loc} = R_z(\psi - \varphi) R_y(\theta) R_z(\varphi) \vec{r} , \qquad \text{[Eq.2]}$$

where $R_y(\theta) = \begin{pmatrix} \cos\theta & 0 & -\sin\theta \\ 0 & 1 & 0 \\ \sin\theta & 0 & \cos\theta \end{pmatrix}$ and $R_z(\varphi) = \begin{pmatrix} \cos\varphi & \sin\varphi & 0 \\ -\sin\varphi & \cos\varphi & 0 \\ 0 & 0 & 1 \end{pmatrix}$ are the rotation matrices about the *y*- and *z*-axes, respectively [1]; and $\vec{r}_{loc} = (x, y, z)^T$ is the coordinates of the point in bead's local frame.

For clarity, we illustrate the bead characterized by the yaw angle θ (positive in the clockwise direction) moving with speed V along an almost straight trajectory that curves with small angular velocity ω (positive in the counterclockwise direction) in **Fig. i.** Angles $\theta = 0$ and $\theta = \pi / 2$ correspond to propulsion in the *parallel* and *perpendicular* orientations, respectively. In other words, a bead's long axis is either perfectly *parallel* or *perpendicular* to the direction of motion.

B. Actin dynamics

The actin network in the comet tail consists of two dynamic actin arrays – transiently attached filaments resisting locomotion, and detached filaments that generate pushing forces. The processes of branching, capping, attachment, and detachment of actin filaments maintain the dynamic equilibrium between these arrays. We simulate a stochastic and spatially explicit version of the tethered ratchet model [2] describing these arrays: new filaments are first randomly created in the attached state at ActA sites that are scattered across the rear half of the bead surface (filaments that appear at the front half would not be incorporated into the tail, and thus, are irrelevant to force generation in the model). Attached filaments detach randomly and then remain detached until they are capped and disappear from the surface of the bead. The respective rates of all processes can be gleaned from the system of equations for the number of attached (n_a) and free (n_f) filaments in the nucleation model:

$$\begin{aligned} \frac{dn_a}{dt} &= k_{nuc}u + k_{att}n_f - k_{det}n_a, \\ \frac{dn_f}{dt} &= k_{det}n_a - (k_{att} + k_{cap})n_f. \end{aligned} \qquad \text{[Eq.3]}$$

Here k_{nuc} = 1000/s is the maximum filament nucleation rate over the bead surface, $u = 1 - (n_a + n_f) / N_{ActA}$ is the fraction of the ActA sites available for nucleating new filaments, N_{ActA}= 2000 is the total number of ActA sites on the bead [2], $k_{att} = 1$/s is the filament attachment rate, k_{det} is the detachment rate of the attached filaments, and k_{cap} = 0.1/s is the capping rate. Based on previous modeling [2], we use the following form for the velocity dependence of the detachment rate:

$$k_{det} = k_{det}^0 \left[1 + \left(V / V_0\right)^2\right] \Big/ \left[1 + \left(V / V_0\right)\ln\left(V / V_0\right)\right], \qquad \text{[Eq.4]}$$

where $k_{det}^0 = 5$ /s is the detachment rate at zero velocity, and $V_0 \approx 50$ nm/s is a characteristic velocity at which the detachment switches from the velocity-independent behavior at slow movement to velocity-dependent one when the bead moves faster.
In the simulations, 2000 ActA sites are evenly distributed on the bead surface with a spacing of approximately 50 nm. We assume a constant pushing filament density across the tail, rather than a constant density over the bead surface. Therefore, we add a projection factor, which is the dot product between the surface normal and the unit velocity vector $\left(-\vec{V} / V\right)$, to the generation rate of free filaments (we use notations $\vec{V}$ for velocity of the bead, and V for the respective speed). The result is that relatively more free filaments push at the rear of the bead, compared to the sides of the bead.

C. Balance of forces and torques

In the 3D model, each detached filament pushes with a force perpendicular to the surface of the bead (**Fig. i,** white solid arrows). These elongating filaments drum on the bead's surface as a result of Brownian motion and thus create a pressure normal to the local surface. Each attached filament pulls in the direction opposite to that of the bead's motion (**Fig. i**, white dashed arrows), which is parallel to the tail's axis. For the pushing filaments, we assume they are all pushing at the stall force

$$\vec{f}_{push}(\vec{r}) = -f_s \hat{n}(\vec{r}), \qquad \text{[Eq.5]}$$

where f_s = 3 pN is the stall force and $\hat{n}(\vec{r})$ is the outward normal unit vector of the ellipsoid's surface. The pulling force is assumed to be proportional to the local velocity of the bead's propulsion [2]:

$$\vec{f}_{pull}(\vec{r}, V, \vec{\omega}) = -k\left(\vec{V} + \vec{\omega} \times \vec{r}\right), \qquad \text{[Eq.6]}$$

where $\vec{\omega}$ is the bead's angular velocity and $k \approx 0.25\ \text{pN}\cdot\text{s/nm}$ is an effective drag coefficient depending on k_{det}^0 and the strength of attachment. Summing up all the pushing and pulling forces from all the attached and detached filaments gives the total force on the bead.

In order to balance the component of the total force that is perpendicular to the tail axis, we assume that a fraction of this sideways force is counteracted by the elastic bending of all attached filaments, while the rest of it is balanced by the local elastic reaction of the actin tail at the very side of the bead (at point A at the edge of the tail; see **Fig. i**). Mathematically, we add the force

$$\vec{F}_{elastic} = -\vec{F}_{\perp} = -\alpha \sum_{\substack{\text{attached} \\ \text{filaments}}} \vec{F}_{\perp} / n_a - (1-\alpha) \sum_{\substack{\text{local detached} \\ \text{filaments near A}}} \vec{F}_{\perp} / n_{local} \qquad \text{[Eq.7]}$$

to the sum of the filament forces in Eqs. 5 and 6. Here $\vec{F}_{\perp}$ is the unbalanced total sideways force, n_a is the total number of attached filaments (the balancing force is distributed equally among them), and n_{local} is the number of detached filaments in a small area at point A at the side of the bead. α is a weight factor which is adjusted to fit the data; good results are obtained for this factor being equal to 0.5.

The sub-piconewton viscous force on the bead ($F_{drag} \approx 6\pi\eta RV \approx 20\times0.01$ Pa·s×1 μm×0.02 μm/s =0.004 pN, where $\eta \approx 10\eta_{water}$=0.01 Pa·s) is negligible since it is much weaker than the filament forces. So, the mechanical condition for the bead's movement is that the total force equals zero:

$$\vec{F}(V, \vec{\omega}) = \vec{F}_{elastic} + \sum_{\substack{\text{attached} \\ \text{filaments}}} \vec{f}_{pull}(\vec{r}, V, \vec{\omega}) + \sum_{\substack{\text{detached} \\ \text{filaments}}} \vec{f}_{push}(\vec{r}, V) = 0. \qquad \text{[Eq.8]}$$

The total torque can be computed by summing up all the cross-products between individual force vectors and the corresponding position vectors in the lab coordinates. The total torque has to be equal to zero:

$$\vec{T}(V,\vec{\omega}) = \vec{r}_A \times \vec{F}_{elastic} + \sum_{\substack{\text{attached} \\ \text{filaments}}} \vec{r} \times \vec{f}_{pull}(\vec{r}, V, \vec{\omega}) + \sum_{\substack{\text{detached} \\ \text{filaments}}} \vec{r} \times \vec{f}_{push}(\vec{r}, V) = 0 . \qquad \text{[Eq.9]}$$

Together, Eqs. 8 and 9 allow finding the speed and angular velocity for the bead in the framework of the lab/actin tail. Because the beads in our experiment are confined in a flat chamber, in our model we further restrict the motion of the bead's centroid in a 2D plane in the lab frame while the bead's rotation is still in a 3D space.

D. Lipid-coated beads

As a lipid-coated bead is propelled forward, molecular complexes that attach to filaments are likely to be 'swept' backward. The distribution of attached filaments therefore becomes significantly biased rearward relative to the distribution of pushing filaments. To simulate this effect, we allow the ActA sites to diffuse on the bead surface, and to be pulled backward by attached filaments. Specifically, the displacement of an ActA site at $\vec{r}$ within a time interval Δt is postulated to be:

$$\Delta\vec{r}_{ActA}(\vec{r}) = \begin{cases} \left[\vec{V} \times \hat{n}(\vec{r})\right] \times n(\vec{r})\Delta t + \Delta\vec{r}_{rand} & \text{if the site is attached,} \\ \Delta\vec{r}_{rand} & \text{if the site is detached,} \end{cases} \qquad \text{[Eq.10]}$$

where $\Delta\vec{r}_{rand} = \sqrt{4 D_{ActA}\Delta t}\cdot\hat{e}$ is the random displacement of the ActA site due to the effective diffusion with the diffusion constant D_{ActA}; $\hat{e}$ is a random unit vector in the plane of the bead surface at position $\vec{r}$. We estimate the value of D_{ActA} from our observation that about 10 % enrichment of ActA is at the rear of the moving lipid-coated bead. By solving the simplified 1D drift-diffusion equation for the ActA density $D_{ActA}[\text{ActA}]'' - v[\text{ActA}]' = 0$ with the approximate values of the velocity and rear/front ratio of the ActA density, we estimate $D_{ActA} \approx 0.01\,\mu\text{m}^2/\text{s}$.

E. Curvature of the bead's trajectory and angular velocity

Fig. ii shows our approach to determining the tail curvature and the resulting angular velocity of the bead's centroid in the lab frame-of-reference. Let us start with points A and B (**Fig. ii, panel A**), which are the left and right boundaries of the tail on the bead surface, respectively. Within the time interval Δt, if the bead rotates with rate ω, then the bead will rotate by an angle $\Delta\theta = \omega\Delta t$ in the counterclockwise direction. As a result, point A will move 'into the tail', while the point B will move 'away from the tail'. We assume that existing filaments at the left edge of the tail can reach and establish contact with some area of the bead that is not previously covered by actin, so that the new tail edge on the left of the bead (A'') is located between the former edge (point A) and the farthermost possible point of contact (point A') of the 'old' existing tail (**Fig. ii, panel B**). Similarly, existing filaments at the right edge of the tail (point B) will have to recede to point B'' if they lose contact with the turned bead in the absence of any actin tail dynamics. Otherwise, the bead's turning could lead to the tail's localization towards the front of the moving bead, in which case the elastic forces in the tail will cause local brakeage and realignment of the tail's boundaries.

We make the assumption that the new boundaries of the tail, A'' and B'', are located in the middle of points A and A' and B and B', respectively, so that the increase of the tail-contacting area on the left equals the decrease of that area on the right (**Fig. ii, panels B, C**). There is no guarantee that the left and right sides of the bead always have the same amount of changes in the areas. More likely, certain force and kinetic balances will predict a numerical ratio between these incremental areas. However, in the absence of an explicit model for these balances, we decide to go with the simplest possibility. Other ratios still give the same sign of the angular velocity.

The locations of A'' and B'' can be obtained from the following two conditions: equal changes in the tail-contacting surface on the left and right of the bead, and tangents to the bead surface at A'' and B'' being parallel to each other (**Fig. ii, panel C**). Then, the change in the direction of tail growth is $\Delta\theta' = \Delta\theta / 2$, which determines the angular velocity of the tail's turning in the lab frame-of-reference to be $\omega / 2$. In the tail frame-of-reference, the angular velocity of the bead, or equivalently, the angular rate of turning of the yaw angle, is also $\omega / 2$. Thus, this model predicts that the angular velocity of the bead's centroid in the lab frame-of-reference and the changing rate of the yaw angle are comparable in magnitude and have the same sign.

In the simulations, the turning of the bead's trajectory is determined by the turning of the tail in the lab frame-of-reference. Since the latter is coupled to the change in the yaw angle, the resulting time-series of these angles give us the relation between the bead's angular velocity and yaw angle.

Results

Linear velocity as a function of yaw angle: Numerical simulations of Eqs. 3-9 predict that the Z-component of pushing force for beads with perpendicular orientations is, on average, 1.2 times of that for beads with parallel orientations. Since a bead's speed, V, is proportional to the pushing force, the ratio of bead's velocity between the two orientations is also about 1.2. This is in semi-quantitative agreement with our observations, according to which the respective speed ratio is close to 1.2.

Lipid-coated beads: We use the 3D model to simulate the *in silico* lipid-coated beads. The results for the yaw angle distribution are in good agreement with the observation data (see **Fig. iii**): the increased motility of ActA on the surface of lipid-coated beads leads to a bias of beads' rotation toward the parallel orientation. This occurs because the points of attachment between filaments and ActA are shifted to the rear, and the rearward force is mostly applied at the rearmost part of the bead. Therefore, a torque is generated to align the bead into its parallel orientation. The resulting angular velocity of beads has greater overall magnitude comparing to that of uncoated beads. The fraction of the yaw angle that is associated with a positive angular velocity, which turns the bead into its parallel orientation, is also higher for lipid-coated beads. Effectively, randomly oriented beads have greater chances to turn into the parallel orientation with greater angular velocities. As a result, more lipid-coated beads move in the parallel orientation, and fewer in the perpendicular orientation compared to uncoated beads.

Frequency of spontaneous yaw angle switching: We observed experimentally that about 89% of beads did not spontaneously switch orientations during the 17 min period of each time-lapse sequence; 9% switched once; and 1.5% switched twice (see **Table 1**, main text). This data fits very well the Poisson distribution for the random, memory-less switching [3] with frequency of about 1/170 min. In the 3D simulations, we find that the frequency of spontaneous switching between parallel and perpendicular orientations is very low (in the range of one per tens of minutes), which is in semi-quantitative agreement with the data (computer-time-consuming nature of the simulations did not allow gathering accurate statistics). Below, we present analytical estimates providing insight into the switching mechanism (Section VII).

II. 2D model of the viscoelastic actin tail with individual filaments at the bead-tail interface

A. Actin dynamics and forces

We model the autocatalytic branching of filaments according to the model previously described in [4]: the total branching rate (1/s/μm×(bead circumference)) is constant, while local filament creation rate is proportional to the local density of existing actin network nodes that are within 200 nm from the bead surface. We also include a spontaneous filament nucleation process with a similar total rate (1/s/μm×(bead circumference)). In the model, filaments are treated in a coarse-grained fashion such that each filament represents an actin array consisting of many individual filaments. We do not track the orientation of each individual filament, because the computer simulation will be highly time-consuming. Instead, we assume that the effective filament arrays are always normal to the local bead surface. We also do not explicitly include the 70 degrees between mother and daughter filaments. When a daughter filament array branches off a mother filament array, we slightly shift its location from the mother array to represent the effective lateral propagation of the branched actin networks [4]. The speed of this shift is chosen to be a random fraction of the free-filament polymerization speed, because the speed of the network propagation should not exceed the polymerization speed of free filaments. The daughter array shifts in a random direction from the mother array along the bead surface, as the direction of the actin propagation is unbiased.

To maintain a persistent bead's motion, we assume that the filament nucleation rate is higher at the rear of the bead compared to that at the front. This effect could result from actin arrays at the front of the bead being swept away by the flow around the bead before the network at the front could mature. We choose the front-to-back ratio of the nucleation rate to be 1:2. Nascent filaments can be in either attached or detached state, with dynamic equilibrium between them; the rates of transition from one state to the other are $k_{att} = 1/\text{s}$ and $k_{det}^0 = 5/\text{s}$. Each newly created filament immediately becomes a part of the existing node-spring network by treating the pointed end of the filament as a new node in the network. Each new node connects to 3 to 4 neighboring nodes within 100-500 nm (respective selection of the nodes is random, but such as not to choose neighbors that are

too close to each other or are in the same direction from the nascent node). Each free filament attaches to the bead surface with a rate $k_{att} = 1/\text{s}$ if its barbed ends is in contact with the bead surface. Each attached filaments can detach from the bead surface and become free with a rate that increases exponentially with the stretching force: $k_{det} = k_{det}^0 \exp(-f / f_0)$ where $f < 0$ is the stretching force on the filament and $f_0 = 1.5\,\text{pN}$ is a force scale. Each free filament gets capped with a constant rate $k_{cap} = 0.1/\text{s}$. When the filament array is capped, the actin network node associated with it is kept until that part of the network disassembles (we choose the disassembly rate to be 0.008 s^{-1}, which corresponds to an average filament lifetime of about 120 s, long enough not to affect the network around the bead). The growth of free filaments follows the Brownian ratchet theory: filament arrays elongate with the rate $v = v_m \exp(-f / f_0)$ where $f > 0$ is the pushing force and $v_m = 50\,\text{nm/s}$ is the free polymerization rate.

Filament arrays are treated as linear elastic springs so that they can exert forces on the bead depending on their deformations. The spring constant for all filaments is assumed to be the same, $k_s = 300$ pN/μm. If a filament array is attached and stretched, it exerts respective pulling force. If the growing end of an array penetrates the bead's surface, the array is considered to be deformed by the penetration length, and so exerting respective pushing force. Forces that exert on the filament arrays automatically apply to the connected node-spring network and cause stress in the network. The deformation of the network, in turn, influences the interactions between the filaments and the bead. In order to model lipid-coated beads, the tangential components of the forces acting on the attached filaments are nullified, while the normal force components are kept. Indeed, the tangential forces simply move ActA attachment points until the forces are relieved.

B. Network dynamics and forces

The actin network of the tail is treated as a node-spring meshwork. Nodes represent the effective network cross-links, while springs represent the deformable actin gel. All springs have the same spring constant, $k_s = 300$ pN/μm, which, considering effective hundreds of nanometers distance between the nodes, corresponds to the effective Young's modulus of the network of the order of 10^3 Pa [5]. When a new node (filament array) is created, all the links that connect it to neighboring nodes are assumed to be un-deformed, with rest lengths being the distances from the node to its respective neighbors. Springs can snap if the stretching force is beyond the threshold value, $f_{br} = 15\,\text{pN}$, representing either actual filament breaking or rupture of cross-links between the filaments. The nodes disappear at a constant rate, $k_{dis} = 0.008\,\text{s}^{-1}$, representing the disassembly of the actin network. The characteristic lifetime of the actin network is therefore $1/k_{dis} \approx 120\,\text{s} = 2\,\text{min}$.

The nodes are moved as follows. The net force that springs applied to the *i*-th node, $\vec{F}_i$, leads to the node's shift by $\Delta\vec{r} = \vec{F}_i / (k_s n_i)$, where n_i is the number of springs connected

to this node. Such shifts are repeated until the all nodes' positions converge to mechanical equilibrium. Furthermore, nodes with a distance to the bead surface greater than a threshold of 1 μm are immobilized. This represents attachment of the older part of the tail to the coverslip. This attachment simplifies calculations considerably, while not affecting the results in a qualitative way because the actin network deformations are important only within the part of the tail closer to the bead's surface than characteristic bead's size.

C. Bead movement

We approximate bead shape with an ellipse of aspect ratio 2. The translational and rotational movements of the bead are determined by the force and torque balances, respectively. During each time step, the displacement and rotation of the bead satisfy the condition that both total force and total torque from all the interacting filaments are zero, exactly as in the 3D model.

Results

Supporting Videos 8 and 9 illustrate that in our simulations the bead is bi-stable, moving either in the parallel or perpendicular orientation, with infrequent switches between the orientations, in agreement with our observations. Simulations of lipid-coated beads show that they are also more likely to move in the parallel orientation. The resulting distributions of yaw angles are reported in the main text (see **Fig. 4B, main text**). Also, the simulations further illustrate that the beads initiate the motility and break through the 'actin cloud', in the parallel orientation, agreeing with our observations.

This result also agrees with theories in [5-7], where respective symmetry breaking is studied for spherical beads and the 'rubber stack' model of symmetry breaking is suggested. According to this model, the first layer of the actin gel grows around the bead in a stress-free manner and forms a thin spherical shell at the bead's surface. Then, a nascent layer of the gel grows at the surface pushing the older actin shell outward. This deforms the outer actin layer so that a tangential stress stretching this outer layer is generated, while the inner layer is compressed radially.

For a fixed gel thickness, the tangential stress at the outer layer is estimated to be proportional to the local curvature of the bead surface [7]. For an ellipsoidal bead, the maximum surface curvature is at the two poles. Therefore, as new actin gel grows from the bead surface, the outer layer near the two poles experiences maximum tangential stress and is most likely to rupture. This local perturbation is unstable: as the actin shell thins out near the poles, the tangential stress of the gel increases at the same location, leading to an exponentially amplified rupture [7] of the actin gel near the two poles. As a result, the actin layer at the poles is thinnest and most vulnerable to fluctuations. When the actin gel ruptures near one pole, the rest of the gel relaxes which greatly reduces the chance of rupture at the opposite pole. The bead will then be pushed out the actin cloud in the parallel orientation through the 'hole' in the gel. Our qualitative observations are consistent with this scenario: before a bead breaks symmetry, the actin fluorescence

around that bead seems to fluctuate for minutes to tens of minutes. When actin starts to thin out and break at one pole, bead's motility starts.

III. Predictions of alternative force-generation models

As a comparison to the 2D viscoelastic model, we simulate separately two 2D models: the simplest variant of the elastic propulsion theory and the tethered ratchet model with a rigid tail that lacks the effect of the elastic forces. The models are built as follows. For the elastic model, we consider, instead of the autocatalytic actin nucleation, a constant nucleation rate (1/s/μm×(bead circumference)) along the bead surface. Because of this condition, effectively constant pushing forces locally normal to the bead's surface are applied at the actin-bead interface, which is similar to the assumption in the elastic propulsion theory. In the tethered ratchet model, we simulate autocatalytic branching, growth, capping, attachment and detachment of hundreds of actin filaments (individual filaments, not effective arrays). The filaments are branched at the proper 70 degrees angle between mother and daughter filaments. The capped filaments are considered rigid and immobile in the lab coordinate system. The uncapped filaments that are in contact with the beads surface are considered to be the elastic rods. We consider actual elastic deformations of such individual filaments. For the free filaments, the boundary condition for the barbed ends is zero tangential forces, and for the attached filaments – fixed coordinates of the barbed ends. Solution of the elasticity theory equations give the elastic forces exerted by each such filament on the bead. To compute the bead's movement, we compute at each step the total force and torque and displace and rotate the bead iteratively until the total force and torque are equal to zero.

The elastic propulsion theory suggests that actin growth generates a radially stretched layer of gel around the bead, and that the bead is squeezed forward by this layer, propped up by more relaxed actin at the rear. This theory implies that the pushing forces are mostly concentrated at the bead poles *A* and *B* (**Fig. i**). With this geometry, such forces exert a torque that will always turn the bead into the parallel orientation. Numerical simulations of this model confirm this intuition: the beads break the stability in the parallel orientation and continue to move in the parallel orientation, as is evident from the **Supporting Video 6**.

Numerical simulations of the tethered ratchet model for the rigid tail, without the effect of elastic forces, show that the bead moves in the perpendicular orientation and never turns into the parallel one, regardless whether new filaments are branched from existing filaments (**Supporting Video 4**) or spontaneously nucleated at the back of the bead (**Supporting Video 5**). The qualitative explanation for this effect is that the bead in a skewed orientation experiences a net force pushing it off the center of the tail, so that at the edge of the bead-tail interface, nascent actin filaments propagate faster along the flatter side of the bead and slower along the curvier side. As a result, the actin network spreads along the more flat half of the bead surface keeping the bead in the perpendicular orientation.

For the lipid-coated beads, both models give the same predictions: as the pulling forces are swept to the rear creating the torque that tends to turn the bead into the parallel configuration, this increases the stability of the parallel orientation in the elastic model, and decreases the stability of the perpendicular orientation in the ratchet model. Obviously, as these two models separately do not predict the bimodal yaw angle distribution, the question about the orientation switching frequency is irrelevant in their frameworks. Finally, the elastic model gives the same prediction about symmetry breaking as the combined model. The ratchet model cannot address this question because of the rigid nature of actin tail in this model.

We consider qualitatively a number of other possibilities as follows. The actin end-tracking model [8] implying yet-to-be-discovered molecular motors at the tips of the filaments leads to the co-localization and, probably, co-alignment of the pulling and pushing forces. It is not clear how to explain any torque under such assumptions. Besides, the greater linear speed of the lipid-coated beads and bias of ActA to the rear of such beads is hard to explain in the framework of this theory, without any spatial separation of pulling and pushing filaments.

Since we observed that there is a faint actin ‘cocoon’ all around the motile beads, we consider the possibility that a strong resistive force originates from continuous ‘breaking’ of the beads through this actin layer. However, semi-quantitative examination of the respective forces failed to explain the bi-stable angular equilibrium of the bead orientation. Besides, beads with both thick and thin actin ‘cocoon’ around them behaved the same.

We also consider the possibility that most of the pushing forces are concentrated at the rearmost point of the bead’s surface and that filaments at the sides are ineffective. However, this scenario leads to the pushing torque invariably turning the bead into the perpendicular orientation, and no assumptions about pulling force distribution are able to restore the bi-stable angular equilibrium of bead orientation.

Finally, one could imagine a peculiar spatial, or even more complex spatiotemporal separation of pushing and pulling forces that would lead to the bi-stable equilibrium in orientation of the motile ellipsoidal beads. For example, if there are more attached filaments at the ‘poles’ and ‘equator’ of the beads, and more pushing filaments at the circular bands between the poles and equator, simulations indicate that the bi-stability is possible. Another possibility is a peculiar dependence of the attachment-detachment dynamics of filament tips on not just the local curvature of the beads surface, but on the derivative of this curvature. However, it is very hard to imagine the biophysical mechanisms that would enable such contrived effects. Similarly, we examine a remote possibility that the pushing forces are aligned with the tail’s axis, or that the pulling forces are not aligned with the tail’s axis, and found that these assumptions do not explain the data either.

IV. Future applications of the hybrid mesoscopic model

The hybrid mesoscopic model is applicable to the force-velocity relation for actin networks growing against rigid surfaces in *in vitro* experiments. It is possible that viscoelastic recoil of the network combines with ratchet forces at the actin-surface interface to produce observed nonlinear and hysteresis-like force-velocity relations. Also, it would be useful to apply the model to the actin network adhering to the compliant substrate and growing against flexible plasma membrane under tension. A number of studies established that retrograde flow of the actin network contributes to the rate of cell protrusion, but the respective viscoelastic effects coupled to individual pushing filaments were never consistently considered.

V. Effect of an actin gel layer around the bead

If the actin gel at front is thin and uniform and the lateral elastic stress is constant in the front gel (**Fig. iv, panel A**), the normal stress will be proportional to the local curvature of the bead (Laplace's law): $f_{\text{res}}=\alpha\kappa$, where α is a constant being proportional to the lateral stress and κ is the local curvature of the bead surface. To calculate the total force F, we define coordinates x'-y' such that the x'-axis is parallel to the front-back boundary AB and the y'-axis is pointing towards the front side of the bead (**Fig. iv, panel B**). We also define ψ to be the angle between the tangent of the bead surface at P and the positive y'-direction. Let ψ_{A} and ψ_{B} be the values of ψ at points A and B, respectively, we have $\psi_{\text{B}} = \pi - \psi_{\text{A}}$. Since $\kappa = \mathrm{d}\psi/\mathrm{d}s$, where s is the arc length along the surface, the x'- and y'-components of total force are

$$F_{\text{res},x} = \int_A^B f_{\text{res}} \cos\psi \, ds = \alpha \int_{\psi_{\text{A}}}^{\psi_{\text{B}}} \cos\psi \, d\psi = 0,$$

$$F_{\text{res},y} = -\int_A^B f_{\text{res}} \sin\psi \, ds = -\alpha \int_{\psi_{\text{A}}}^{\psi_{\text{B}}} \sin\psi \, d\psi = -2\alpha \cos\psi_{\text{A}} < 0.$$

The total resisting force F_{res} is always along the negative y' direction, which is always perpendicular to line AB and points towards the back of the bead.

The total torque produced by the compression forces about the bead's center is zero. This can be seen in **Fig. iv, panel A**. Let point C be the symmetric point of A about the bead's long-axis. Because of the symmetry, the torque from compression forces between A and C is zero, and the torque from compression forces between B and C is also zero. Thus, the total torque from the compression forces at the front is zero. Similar argument shows that if the origin of the force is not elastic but pushing from ratchet mechanism, the total torque would be zero.

The resisting force, however, will affect the bead's torque balance indirectly. That is because F_{res} typically has a component along the short-axis of the bead, which is against the sideways pushing force from the tail and helps relieve the local elastic force. As a result, the torque from F_{elastic} is smaller, which reduces the tendency of bead's moving along its long-axis. Therefore, the existence of a thin gel at the front of the bead tends to align the bead to move along its short-axis. If the origin of the force is from the ratchet

mechanism, then the effect discussed in this paragraph slightly reduces the bias toward the orientation along the bead's short axis.

If the actin gel covering the front of the bead is non-uniform, it is likely to generate a torque on the bead. One possibility is that gel exists when the angle between the surface normal and v is greater than a certain critical angle ϕ_c (points C and D in **Fig. iv, panel C**). This could result from the "brushing" of the surrounding fluid on the gel. If the gel between points C and D exists, the total torque from the front gel is zero. Since the gel between C and D produce a torque that turns the bead to the perpendicular direction (τ^* in **Fig. iv, panel C**), the torque from the rest of the front gel should align the bead to move along its long-axis. This conclusion remains the same whether the force is produced by elastic or ratchet mechanism.

The other possibility is that gel at front tends to rupture near highly-curved surface due to high lateral stress. Then, the thinning of gel is symmetric about the long-axis of the bead. The resulting force and torque are zero, having no impact on the orientation of the bead. From this analysis, we conclude that gel at front of the bead may have different impact on the orientation of the bead, depending on the property and configuration of the gel, but as long as the gel is thin, the influence is likely to be small.

VI. Temporal sequence of changes in motion, orientation, and actin density

In the following text we qualitatively explain the observed sequence of events: turning or change in direction in the bead's trajectory (angular velocity) → actin accumulation on the inner side → change in bead orientation with respect to the comet tail (yaw angle).

The number of attached filaments is significantly smaller than that of free filaments, and so the relative fluctuations of number of the attached filaments are expected to be significant. This leads to fluctuations in the attached/free filament ratio that causes unbalanced forces and growth speeds at the two sides of the bead. Specifically, the side with a higher fraction of attached filaments will move slower than the other side, causing the trajectory turning. We suggest that this consequence of the fluctuation of the attached filament number is the beginning of the sequence of the observed changes.

As the bead changes direction and curves in its trajectory, the inner side of the bead moves more slowly than the outer side, resulting, according to the model, in a lower filament detachment rate and thus in a higher density of attached filaments on the inner side of the bead. In addition, the slower relative motion between the inner bead surface and the tail reduces the effect of the free filaments growing past the surface and 'leaving' it, further increasing the filament density at the inner side. The time lag between the trajectory turning and the accumulation of actin at the inner side of the bead is roughly the actin network turnover time, which is estimated to be about 20 s, consistent with the experimental observation.

Next, the redistribution of the actin density around the bead will lead to the bead's reorientation relative to the tail, after the oscillation of the attached/free filament ratio is reduced. The reorientation of the bead with respect to its tail is driven by both the torque and the reorientation of actin tail along the bead surface. The speed of turning is also affected by the resistance from the actin gel around the bead: the bead needs to move through the cocoon of existing gel before it can turn. Thus, changes in yaw angle happen after changes in the direction of a bead in a trajectory and actin redistribution. For a bead moving at a speed of 30 nm/s, the time required to advance a sub-micron distance (a fraction of the bead's size) is on the order of 10 s. We estimate that the time lag for the change of yaw angle is comparable to this time interval, which is consistent with the observed 10 s delay.

VII. Frequency of bead orientation switching

Bead orientation switching between the parallel and perpendicular orientation can be explained as follows. In addition to the turning from torque and geometric effect, there is turning caused by fluctuation in the actin networks. Considering N filaments pushing against the bead rear surface, the fluctuation in filament numbers from the left to the right sides of the bead is about $\sqrt{N}$. On average, these fluctuating filaments tend to push the bead at an angle of $\pi/4$ away from the current direction of motion, causing random turnings of the bead, while the rest filaments push the bead along its previous direction. The net angular change in the direction of motion is $\Delta\theta \sim (\pi/4)(\sqrt{N}/N) = \pi/4\sqrt{N}$. The duration of this bias is related to the actin turnover time τ_0, which is obtained from stability analysis of Eq. 3. The rotational diffusion constant for this turning can be estimated as $D = \Delta\theta^2/2\tau_0 \sim \pi^2/32N\tau_0$. With actin fluctuation alone, the average time for a bead to reach halfway of the orientation-switching is $t_0 = (\pi/4)^2/2D \sim N\tau_0$. The relative rotation between the bead and its tail is also affected by both the torque from the tail and the reorientation of the actin tail along the bead surface. Since the orientation of beads have bi-stability, the angular velocity of the bead with respect to its tail can be approximated as $\omega \approx \omega_0 \sin(4\theta)$, meaning that beads with $0 < \theta < \pi/4$ tend to rotate towards its long-axis while beads with $\pi/4 < \theta < \pi/2$ tend to rotate towards its short-axis. Therefore, the total time for a bead to achieve half of the orientation switching can be estimated from the Arrhenius equation (assuming effective diffusion-drift process in the angular space): $t = t_0 \exp\left(\frac{1}{D}\int_0^{\pi/4} \omega\, d\theta\right) \approx N\tau_0 \exp(16N\omega_0\tau_0/\pi^2)$, where the exponent in the second term represents the maximum "barrier height" for the rotation. For the beads with $N \approx 900$, $\omega_0 \approx 0.1$ deg/s and $\tau_0 \approx 1\,\text{s}^{-1}$, we get $t \sim 100 - 200$ min, which agrees well with the observed time interval for switching t ~ 170 min.

VIII. Bead orientation during symmetry breaking

The differences between our finding that the bead starts moving and breaks through the symmetric layer of actin gel in the parallel orientation and a previous published observation [9] can be due to experimental differences. First, this previous study [9] involved a reconstituted system consisting of purified proteins, which probably had slower actin depolymerization dynamics than the cytoplasmic extracts used in our study. Because of the faster actin depolymerization rate in our case, the elastic stress in the network decreases faster and the stress can be more local, not spreading across the whole bead-actin interface. If this is the case, the local elastic stresses correlate with local interface curvature, which is highest near the bead's poles, where we observe the symmetry breaking. If the stress spreads more globally in the case reported in [9], then the local curvature variations matter less than the hoop stress that develops around the bead's 'equator' and dominates stresses in all other directions. Such hoop stress, as was shown in [9], leads to the linear break along the long axis of the bead at its more flat side and emergence of the bead from the actin cloud in the perpendicular orientation.

The second reason could be differences in geometry. In our study, ~1 μm beads are confined in a slide-chamber only ~2 μm deep. But in [9], ~5 μm beads are placed in a 15.5 μm deep chamber. The ratio of the chamber depth to the bead size is 2 in our case and 3 in [9]. Therefore, we argue that beads in our study are confined in a quasi-2D environment, while those in [9] are in a more 3D environment. Our 2D simulations predict the symmetry break in the parallel configuration, and this geometry resembles the experimental configuration of the current study more closely. The symmetry breaking process is more 3D in [9], and the 3D model used in [9] indeed predicts symmetry breaking through the actin cloud in the perpendicular orientation, because the dominant hoop stress in the actin gel is essentially a 3D phenomenon.

IX. Rapid trajectory turning behavior of lipid-coated beads

In the text, we have a qualitative explanation for the observed faster angular speed of lipid-coated beads. This explanation is based on the spatial separation between the maxima of the ActA distribution (which is at the rear pole of the bead) and of the actin distribution (which is skewed to the inner side of the bead relative to the trajectory). Our model can produce such separation only transiently and briefly, at which moment the angular velocity is high. However, for most of the time, the model predicts nearly symmetric (with respect to the long axis of the bead) distributions of both ActA and actin, and lower angular velocities. We hypothesize that this quantitative discrepancy between the observations and modeling predictions is because we have very simple detachment kinetics of the actin-ActA links in our model. More complex and nonlinear force-dependence of respective detachment rates can, in principle, lead to a much discussed 'stick-slip' properties of the attachments. More specifically, actin-ActA links can detach cooperatively, not one by one, but all at once, so the bead at any given moment is either attached in many places to the actin network, or is almost detached, and there is a rapid back and forth switching between these two states. Indirect data from two studies has pointed to such kinetics [10,11]. If this is indeed the case, a spatial separation during the

fraction of the time the bead is attached would occur and rapid turning would ensue, as described above. This turning would lead to a skewed actin distribution. The resulting positive feedback between actin redistribution, turning and attachment state could lead to the turning state becoming steady and persistent. In our current model this does not happen, but preliminary estimates show that this can happen if the force-dependence of the detachment rate is more nonlinear. We will explore this possibility in the future. Also, it is very likely that if ActA is immobile, any inhomogeneous distribution at the bacterial or bead's surface will cause rapid turns.

References

1. Goldstein H, Poole C, Safko J (2001) Classical mechanics. 3rd ed. Addison-Wesley.
2. Mogilner A, Oster G (2003) Force generation by actin polymerization II: The elastic ratchet and tethered filaments. Biophys J, 84: 1591-1605.
3. Berg HC (1993) Random Walks in Biology. Princeton, New Jersey: Princeton University Press.
4. Lacayo CI, Pincus Z, VanDuijn MM, Wilson CA, Fletcher DA, et al. (2007) Emergence of large-scale cell morphology and movement from local actin filament growth dynamics. PLoS Biol 5: e233.
5. Noireaux V, Golsteyn RM, Friederich E, Prost J, Antony C, et al. (2000) Growing an actin gel on spherical surfaces. Biophys J 78: 1643-1654.
6. Plastino J, Olivier S, Sykes C (2004) Actin filaments align into hollow comets for rapid VASP-mediated propulsion. Curr Biol 14: 1766-1771.
7. Sekimoto K, Prost J, Julicher F, Boukellal H, Bernheim-Grosswasser A (2004) Role of tensile stress in actin gels and a symmetry-breaking instability. Eur Phys J E Soft Matter 13: 247-259.
8. Dickinson RB, Caro L, Purich DL (2004) Force generation by cytoskeletal filament end-tracking proteins. Biophys J 87: 2838-2854.
9. Dayel MJ, Akin O, Landeryou M, Risca V, Mogilner A, Mullins RD (2009). In silico reconstitution of actin-based symmetry breaking and motility. PLoS Biol, 7: e1000201.
10. Soo FS, Theriot JA. (2005) Adhesion controls bacterial actin polymerization-based movement. Proc Natl Acad Sci U S A. 102:16233-16238.
11. Alberts JB, Odell GM. 2004. In silico reconstitution of Listeria propulsion exhibits nano-saltation. PLoS Biol. 2:e412.

Fig. i

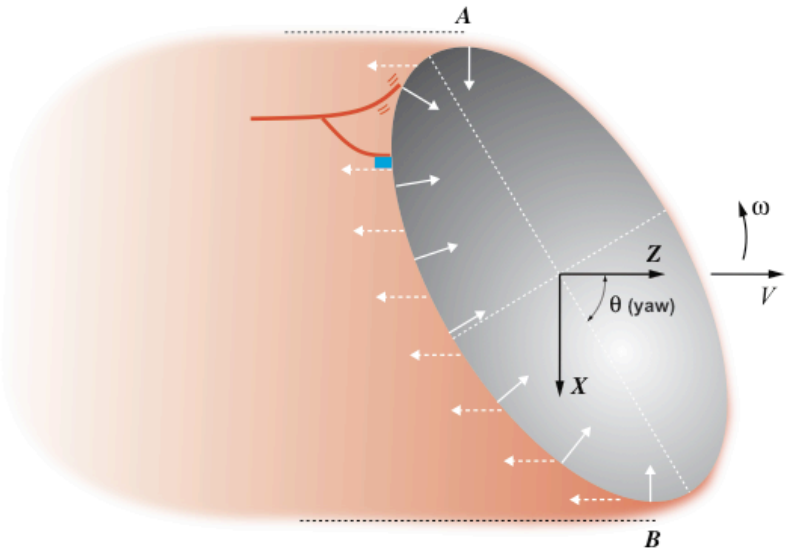

Figure i: Schematic illustration of the model. An ellipsoidal bead is represented by an ellipse with an aspect ratio of 2. Attached filaments apply forces that are on average opposite to the direction of movement and parallel to the comet tail (white dashed arrows). Pushing filaments generate forces directed normal to the surface of the bead (white solid arrows). Bent elongating filaments (top red line) 'drum' on the surface of the bead as a result of Brownian motion and create a pressure directed normal to the surface. Pulling filaments (bottom red line) can transiently attach to molecular complexes (blue rectangle) on the surface creating forces that oppose the forward movement of the bead. Yaw angle=θ, angular velocity=ω, V=speed, A and B are side-to-side comet tail boundaries.

Fig. ii

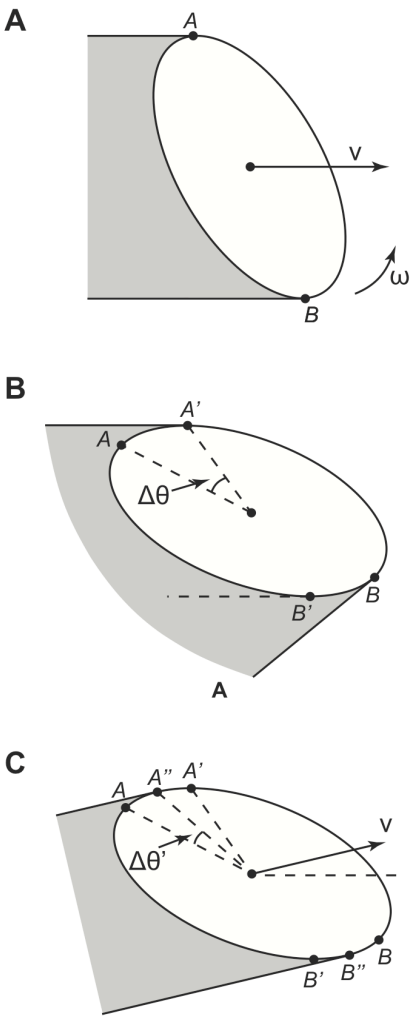

Figure ii: Schematic illustration of the tail's rotation. (A) Before the bead's rotation, points *A* and *B* – edges of the tail – are on opposite sides, on the left and right of the bead. In this schematic the bead is depicted migrating from left to right with a linear speed *V*. Δt represents the time interval. The bead changes direction of movement with the rate ω in the counterclockwise direction. (B) As the bead changes direction, the bead also rotates by the angle $\Delta\theta = \omega\Delta t$ in the counterclockwise direction. In this intermediate stage, point *A* moves to *A′*, while point *B* stays at the same position on the surface of the bead. (C) The tail 'shrinks' so that its new edges, points *A″* and *B″* determining the direction of motion, do not hinder the bead's propulsion.

Fig. iii

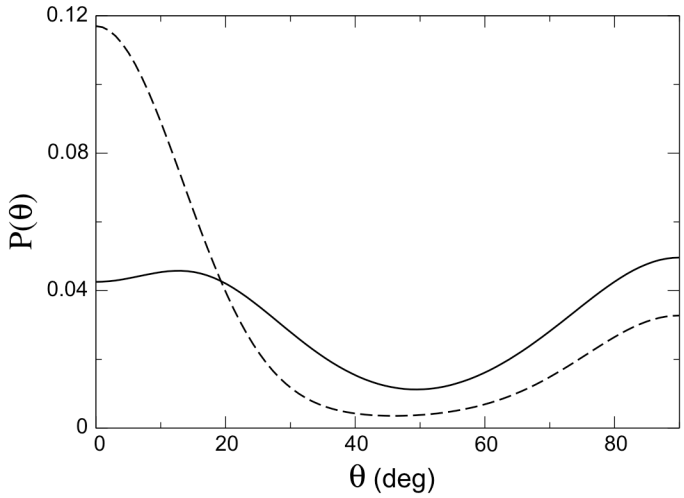

Figure iii: Computed distribution of yaw angles for uncoated (solid line) and lipid-coated beads (dashed line) in the 3D model.

Fig. iv

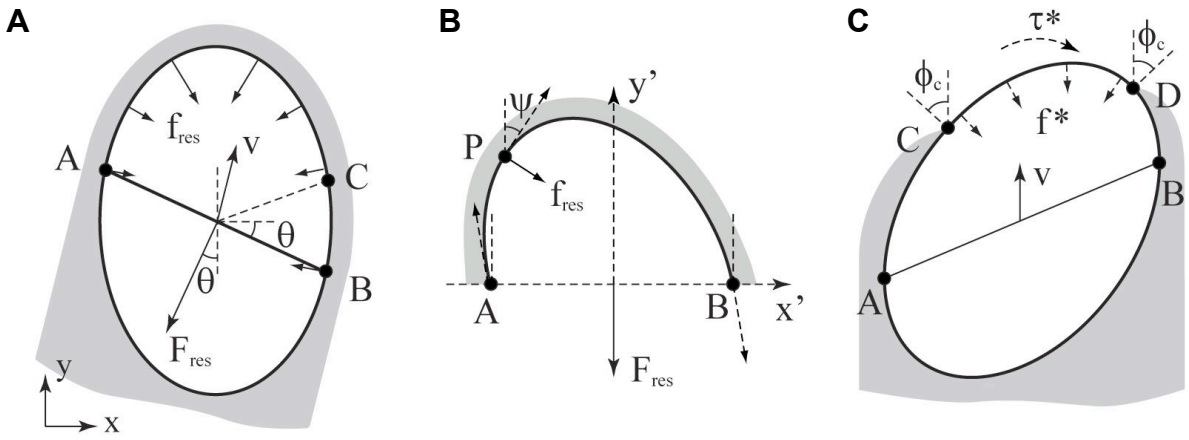

Figure iv: Influence of the actin gel at the front of the bead. (A) Schematic of an ellipsoidal bead surrounded by a uniform gel, including the front of the bead is shown in bead frame-of-reference. A and B are points on the bead where tangents are parallel to v. (B) The front half of the gel in the x'-y' frame-of-reference. (C) Partial actin gel at the front in the tail frame-of-reference. The actin gel exists only if the angle between the surface normal and v is greater than a critical angle ϕ_c (between C and D). The torque from the missing actin gel between C and D is τ*.